Volume 12
Number 11
7 June 2022
Pages 3375–3738

Catalysis Science & Technology

rsc.li/catalysis

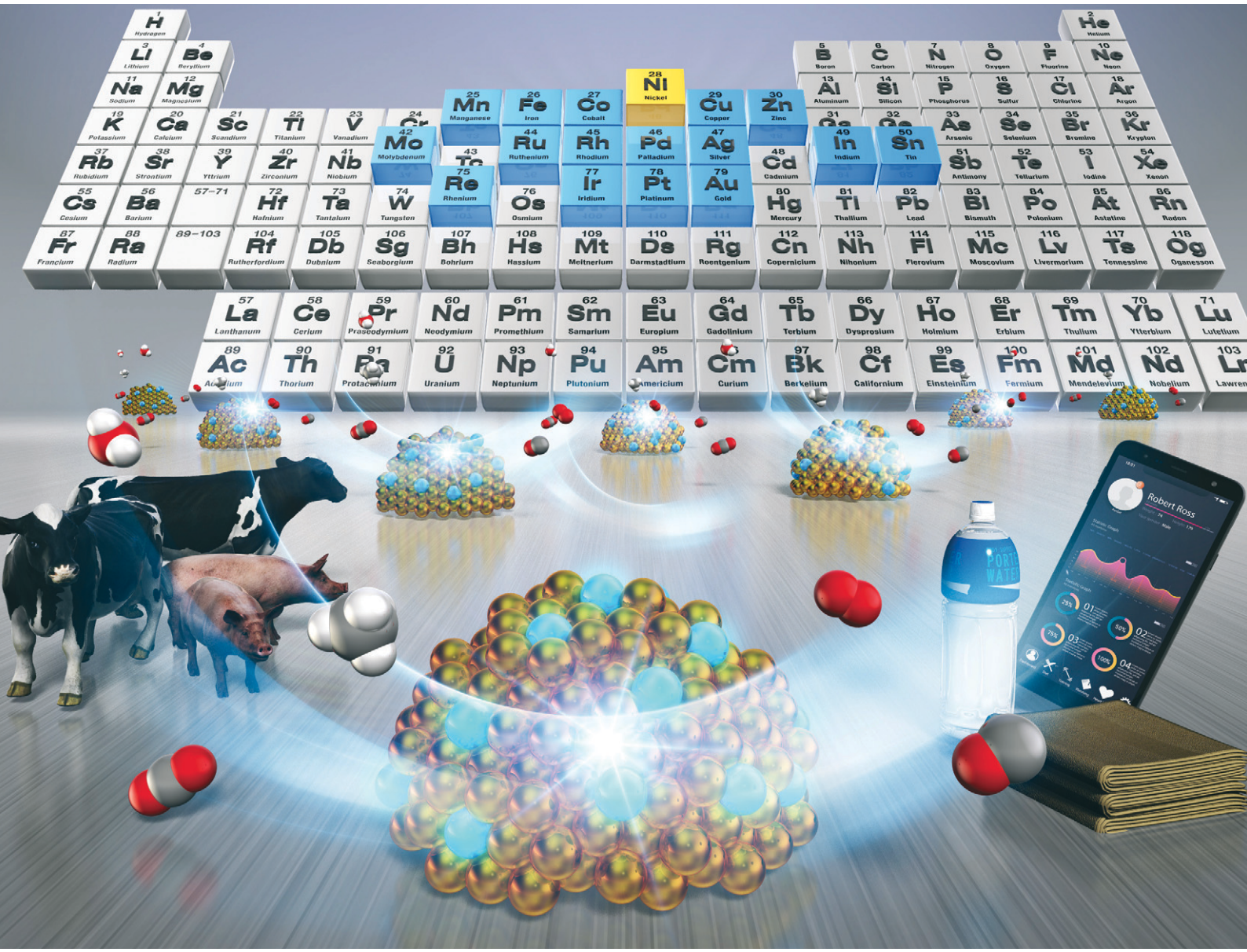

ISSN 2044-4761

ROYAL SOCIETY OF CHEMISTRY

MINIREVIEW

Maki Torimoto and Yasushi Sekine
Effects of alloying for steam or dry reforming of methane: a review of recent studies

Catalysis Science & Technology

ROYAL SOCIETY OF CHEMISTRY

MINI REVIEW

View Article Online
View Journal | View Issue

Cite this: *Catal. Sci. Technol.*, 2022, **12**, 3387

Effects of alloying for steam or dry reforming of methane: a review of recent studies

Maki Torimoto and Yasushi Sekine *

Methane is an important chemical resource, not only in natural gas but also in biogas, which can be regarded as a renewable energy resource. Reforming of methane with steam or carbon dioxide, which is important for producing hydrogen and syngas, is conducted at high temperatures using heterogeneous catalysts. To achieve high activity, stability, and low carbon deposition, many studies have been conducted in recent years on the use of alloys as active sites in these catalysts. This review presents a summary of recent studies of alloy catalysts, for which various secondary metals have been added to active metals, such as Ni. Then we summarize the current status of these alloys in terms of their structure, electronic state, and adsorption. The reported effects of alloying include improvement of dispersion and reducibility of the supported metal, change in catalytic performance such as activity and selectivity, and improvement of durability against carbon deposition, sulphur poisoning, and sintering. The directions of future research and development are summarized in terms of sulphur resistance, sintering inhibition, and high activity at low temperatures.

Received 12th January 2022,
Accepted 18th February 2022

DOI: 10.1039/d2cy00066k

rsc.li/catalysis

1. Introduction

1.1 Roles of alloys for catalysis

Supported metal catalysts have been used widely in various chemical processes up to the present day. The supported metal catalyst activity varies depending on the metal particle size, shape, structure, composition, electronic state, and so on.[1] Therefore, increasing the catalyst activity and selectivity by controlling the structure, composition, and electronic states of supported metals is important for developing high-performance catalysts. In this sense, alloy catalysts, in which the original metal is intermixed with second, third, or more metals, have been studied widely as one method of modifying the properties of supported metals.[2–4] Bi-metallic catalysts have various mixing states: a random solid-solution alloy, an intermetallic compound (IMC), a surface alloy, alloys with a core–shell structure, and others.[5] Solid-solution alloys are classifiable into two types: substitutional and interstitial alloys. The former is an alloy in which substitution of metals occurs when the second metal has similar characteristics, such as the size or electronic properties, as the original metal. The latter is an alloy for which the second metal is sufficiently small to incorporate with the lattice void of the original metals. Unlike these random alloys, IMC has an ordered structure comprising two metal elements, yielding a crystal structure that differs from that of the mother metal.[2,5] As for the bi-metal system of bulk, the change in the Gibbs free energy of mixing is often used to explain the mixing state of the two metals. The change in Gibbs free energy of mixing, ΔG_{mix}, is calculable using the change in enthalpy, ΔH_{mix}, and in entropy, ΔS_{mix} during alloy formation (eqn (1)).

$$\Delta G_{mix} = \Delta H_{mix} - T\Delta S_{mix} \quad (1)$$

If ΔG_{mix} is negative, then a random alloy or intermetallic compound is formed spontaneously in the mixing condition. The sign and the magnitude of the ΔH_{mix} value are important because ΔS_{mix} is assumed to be positive.[2] If the bond formation between the original metal and the second metal is exothermic ($\Delta H_{mix} < 0$), then ΔG_{mix} is always negative and alloy formation occurs spontaneously. However, if the bond formation between the original metal and the second metal is endothermic ($\Delta H_{mix} > 0$), formation of the alloy depends on temperature. At high temperatures, the contribution of $T\Delta S_{mix}$ is sufficiently large to make ΔG_{mix} negative. However, at a low temperature, ΔG_{mix} is expected to be positive, which causes separation of the formed alloy. Furthermore, the transition from a random solid-solution alloy to an intermetallic compound can be estimated using eqn (1).[2] Considering the transition from disorder to an ordered structure, ΔS_{mix} is expected to be negative. Therefore, the transition is entropically unfavourable. By contrast, ΔH_{mix} would be a large, negative value because of the stronger intermetallic bond energy. Therefore, whereas the low-temperature condition is favourable for the formation of intermetallic compounds, the high-temperature condition produces a disordered structure.

Applied Chemistry, Waseda University, 3-4-1, Okubo, Shinjuku, Tokyo 169-8555, Japan. E-mail: ysekine@waseda.jp

In recent years, alloys of some new types, such as single-atom alloys (SAAs)[6,7] and high entropy alloys (HEAs),[8,9] have received much attention. The former, SAAs, are alloys in which a very small amount of the second metal, such as 1 : 10 or 1 : 100, is added to the original metal. The second metal atoms are atomically dispersed on the original metal surface. In many SAA systems, a small amount of 8, 9, or 10 group metal (Pd, Pt, Rh, Ni, Ru, *etc.*) is added to the 11 group metals (Cu, Ag, Au).[7] Earlier studies of SAAs have reported numerous benefits, including higher activity or selectivity, increased stability for coke formation, and increased stability for CO poisoning. In research in this field, STM investigations using a single crystal substrate have been conducted widely, in addition to XAFS and HAADF-STEM measurements.[7] The latter type mentioned above, HEAs, are generally categorized as alloys comprising at least five nearly equimolar metal components (5–35 atom % for each component), although the definition remains controversial.[8,9] Because configurational entropy increases as the number of components increases, HEAs have high stability (the high entropy effect). Reportedly, HEAs show interesting and unexpected catalytic performance for various reactions.

Effects of alloys on modifying the metal properties are often explained with two terms: ligand effect and ensemble effect.[3,10,11] The ligand effect represents changes of the electronic structure caused by electron transfer between the original metal and the second metal. The ensemble effect represents a geometric effect by which the ensembles of active metals are diluted by the addition of second metals. The ensemble effect can suppress undesired side reactions such as coke formation. Nevertheless, it sometimes engenders decreasing activity of the main reaction when ensembles of active metals are necessary for activating reactants.[3] Therefore, the metal components should be chosen carefully depending on the purpose.

As described above, alloys have numerous benefits, including increased catalytic activity, selectivity, and stability for various catalytic reactions. However, the role of the second metal is expected to be different for each reaction. It cannot be understood simply by a general explanation. For this review, we specifically examine the steam and dry reforming reaction of methane to gain a deep and comprehensive understanding of alloy effects.

1.2 Increasing demand for chemical usage of methane

The use of CH_4 as a new alternative energy source and as a chemical material source instead of crude oil has become popular.[12–15] Actually, CH_4 is the main component of natural gas, shale gas, and bio-gas by fermentation.[16] The chemical utilization of CH_4 includes steam reforming of CH_4 (SRM), dry reforming of CH_4 (DRM), partial oxidation of CH_4 (POM), autothermal reforming (ATR), and oxidative coupling of CH_4 (OCM). Among these, SRM is the most commonly used process to produce H_2; DRM is important for the effective utilization of greenhouse gases by converting CH_4 and CO_2 into industrially important syngas, a mixture of CO and H_2. In fact, according to the Sixth Assessment Report (AR6) of the Intergovernmental Panel on Climate Change (IPCC) published in 2021, the gases exerting the strongest greenhouse effect are CO_2, CH_4, and N_2O, in that order. Therefore, improving the methane reforming process efficiency to reduce the amount of CO_2 emitted and to use greenhouse gases for chemical production is expected to become increasingly important for building a sustainable society. According to the International Energy Agency's (IEA) Energy Technology Perspectives 2020, 75 Mt of hydrogen are produced each year from natural gas (76%) and coal (23%). They are used for industrial applications such as oil refining (33%) and ammonia synthesis (27%).

SRM is a process to produce hydrogen from CH_4 (eqn (2)). Water gas shift (WGS) occurs sequentially, thereby increasing the H_2 yield (eqn (3)).

$$CH_4 + H_2O \rightarrow CO + 3H_2 \quad \Delta H^0_{298} = +206 \text{ kJ mol}^{-1} \tag{2}$$

$$H_2O + CO \rightarrow CO_2 + H_2 \quad \Delta H^0_{298} = -41 \text{ kJ mol}^{-1} \tag{3}$$

Although SRM has a long history and although it is a mature process, many issues remain to be resolved.[13–15,17–23] First, industrially, SRM is conducted under high-temperature and high-pressure conditions such as 1000–1300 K and 3–25 bar, because of the stability of CH_4 and a large endothermic reaction. Such harsh conditions lead to consumption of huge amounts of energy, requiring high costs because of the need for heat exchangers and heat-resistant materials.[22] Next, Ni catalysts, which are mainly used industrially, deactivate easily because of coke formation, sintering, and poisoning by impurities such as S species in the feedstock. Noble metal catalysts (Pd, Rh, Ir, Ru, Pt, *etc.*) exhibit not only high activity but also high durability.[22] However, because of their high cost, noble metal catalysts have not yet been industrialized. Therefore, development of a catalyst that can operate efficiently with high durability at low temperatures is desired in SRM.

The DRM process produces syngas, a mixture of CO and H_2, from CH_4 and CO_2, as described in eqn (4).[24–28] Sequentially, a reverse water gas shift reaction (RWGS) occurs (eqn (5)).

$$CH_4 + CO_2 \rightarrow 2CO + 2H_2 \quad \Delta H^0_{298} = +247 \text{ kJ mol}^{-1} \tag{4}$$

$$CO_2 + H_2 \rightarrow CO + H_2O \quad \Delta H^0_{298} = +41 \text{ kJ mol}^{-1} \tag{5}$$

Syngas is a raw material for various chemical reactions such as FT synthesis, methanol synthesis, and DME synthesis.[28] Although DRM is an attractive reaction, its commercialization has been hindered by difficult challenges, which are almost identical to those for SRM: the requirement for high temperatures (over 1000 K) and rapid catalyst deactivation. Furthermore, DRM has a higher ratio of C to H than SRM, which makes it more prone to carbon formation.

1.3 Contents of this review

As described earlier, SRM and DRM have similar directions and issues to be developed. In both cases, the needs for high temperature and the catalyst durability are important issues. Many methods to improve activity, selectivity, and stability, have been reported. However, this review specifically examines methods to control the properties of the supported metals for thermal catalytic SRM and DRM and provides a detailed and comprehensive summary. In recent years, comprehensive review papers on SRM have been reported by Zhang *et al.*[23] in 2021 and by Chen *et al.*[22] in 2020. However, no report of the relevant literature describes a study of alloys. Many review papers of recent years have described DRM.[24–35] Among these papers, Aziz *et al.*[27] and Yentekakis *et al.*[25] respectively produced reviews for bimetallic catalysts in 2020 and 2021. Bian *et al.*[26] presented a review for nickel-based alloys in 2017. The present review assesses effects of alloys in SRM and DRM, with depth and breadth of comparison and with verification of the similarities and differences between the two reactions.

2. Properties of metals that exhibit high activity for SRM and DRM

The order of catalytic activities on active metals for SRM has been reported as shown below.[36,37]

$$Rh > Ru > Ni > Ir = Pd = Pt > Co > Fe$$

In addition, Ferreira-Aparicio *et al.*[38] calculated the TOF in DRM for various metals and showed that the order differs for Al_2O_3 support and SiO_2 support. The order of TOF of the methane reaction rate on each support is presented below.

$$Ni > Ru > Rh, Ir \quad (SiO_2 \text{ support})$$

$$Rh > Ni > Ir > Pt, Ru > Co \quad (Al_2O_3 \text{ support})$$

For SRM and DRM, it is common to use Ni catalysts, which are active and inexpensive, supported on metal oxides such as Al_2O_3, which have high heat resistance.[21,39] Other popular supports include durable $MgAlO_x$ support, mesoporous materials with high specific surface area, CeO_2 base support with high oxygen storage capacity, and perovskite oxide support.[40] However, Ni catalysts are prone to carbon deposition, sintering, and sulphur poisoning. Catalyst development is therefore still ongoing. Noble metal catalysts are more active. They have the salient advantage of being less prone to carbon deposition than Ni catalysts, but they are expensive and difficult to use industrially.[41] Table 1 shows prices for various metals as of December 2021, showing that the prices of noble metals are much higher than that of Ni. The most popular research is therefore to use the Ni catalyst as a basis for improving catalytic performance by improving the performance of supports and metals.

Table 1 The recent average prices of precious and base metals as of 2021 by Tanaka Precious Metal

Metal	Pt	Au	Ag	Pd	Rh	Ir	Ru
$ per g	33.7	58.7	0.8	83.4	608.3	168.3	23.5

The rate-limiting step in SRM is reportedly dissociative adsorption of CH_4, *i.e.*, cleavage of the C–H bond of CH_4 that occurs on a metal surface.[42–45] In DRM, the mainstream theory is that the CH_4 activation occurs on the metal, but it is generally accepted that activation of CO_2 might occur on the metal or the support depending on the catalyst and operating conditions.[46] Therefore, the key steps in the DRM process mechanism are regarded as being the adsorption and dissociation of CH_4 on the metal site, adsorption and dissociation of CO_2 on the support or the metal site, or both. Details of the DRM reaction mechanism have been summarized in reports by Yentekakis *et al.*,[25] Fan *et al.*,[40] and Ranjekar and Yadav.[46]

Details of the structure dependence of these reactions were investigated by Vogt *et al.*[47] in 2020. Fig. 1 presents the possible reaction pathways on metals in SRM and DRM. Activation of H_2O and CH_4 requires σ-bond cleavage, whereas the activation of CO_2 requires π-bond cleavage (Fig. 1(a)). An important point here is that the sites with higher activity for C–H activation and C═O activation might be different. Reportedly, C–H cleavage occurs preferentially at co-ordination-unsaturated sites, whereas π-bond activation and cleavage occur preferentially at defect sites. Therefore, these reactions might have different active sites. Fig. 1(c) shows the general relation between supported metal particle size and TOF, where class 1 is for structure insensitivity, class 2 is for π-bond structure sensitivity, and class 3 is for σ-bond sensitivity. In class 2, the TOF is classified further as increasing and then decreasing or remaining constant. When the rate-limiting step involves the activation of a σ-bond, such as a C–H bond, it is usually shown as class 3 in Fig. 1(c). In this class, the TOF generally increases as the size of

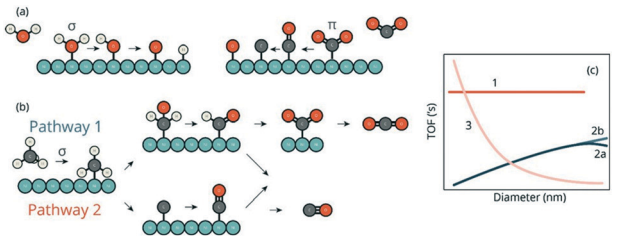

Fig. 1 (a) The σ-bond cleavage is necessary for activation of H_2O or CH_4, and the π-bond cleavage is necessary for CO_2 activation. (b) Possible two pathway for SRM and DRM; pathway 1 is a formyl-intermediate route and pathway 2 is a direct carbide route. (c) General classification of TOF dependence of metal particle diameter. Class 1 is for structure insensitivity, class 2 is for π-bond structure sensitivity, and class 3 is for σ-bond structure sensitivity. Reprinted with permission from ref. 47. Copyright 2019 American Chemical Society. https://pubs.acs.org/doi/10.1021/acscatal.9b04193.

the metal nanoparticles decreases because the reaction proceeds predominantly on the co-ordination-unsaturated side. However, when the C═O cleavage is rate-limiting, a certain amount of site co-ordination is required, which is classified as class 2. Consequently, pathway 1 (Fig. 1(b)) might be much more predominant for catalysts where C–H activation is difficult, whereas pathway 2 might be predominant for catalysts where the recombination of C and O adatoms is very slow compared to the activation of C–H bonds.

However, the Ni particle size dependence of TOF in SRM and DRM investigated using 1–6 nm Ni/SiO_2 catalysts differs slightly from the general classification as shown in Fig. 1(c). Catalysts supporting very small Ni particles (<1.5 nm) were less active: maximum activity was achieved at 2–3 nm of metal particle. This might be true because the balance of active sites for σ-bond and π-bond is important. A combination of different sites is necessary. In addition, the isotopically labelled experiments showed that the CH_4 activation is not the only rate-determining step. Results suggest that the formation of CO by recombination of C and O and that the desorption of CO are likely to be important kinetically limiting factors for both SRM and DRM.

Furthermore, earlier reports show that CH_4 activation requires an ensemble of active metals rather than a single active metal atom.[17,48] Rostrup-Nielsen[17] reported in 1984 that three Ni atoms are involved in the reaction. Rocha *et al.*[48] reported in 2019 that two adjacent Ni atoms are necessary for CH_4 activation. It is often discussed that when the active site is an ensemble of active metals, the ensemble effect, in which the second metal dilutes the ensemble of active metals, engenders a decrease in the activity.[3] However, ensemble dilution is highly effective at inhibiting coke formation (details are presented in chapter 3). Numerous reports have described important improvements in stability achieved by adding small amounts of the second metal.

Catalytic activity is often expected to correlate with the electronic state of the metal surface or d-band centre.[49–51] Such explanations using DFT calculations have been reported also for CH_4.[45] Abild-Pedersen *et al.*[45] reported the correlation between the surface d-band centre and the transition state energy of CH_3–H bond dissociation. Consequently, it is expected that if the d-band centre is increased by alloying, then the activity would be higher. If the d-band centre were decreased by alloying, then the activity would be lower. Recently, Joo *et al.*[52] associated the high activity of CoNiFe ternary catalyst in DRM to the d-band centre of the metal. However, they reported the existence of an optimal d-band centre value. Roy *et al.*[42] also compared surface properties such as surface energy, work function, and density of states of Ni–Pt alloy with the activation barrier for methane dissociative adsorption, concluding that, among the surface parameters, the d-band centre can be relied upon as a descriptor for predicting the trend of activation energy for CH_4 dissociation in some alloy systems. Ray *et al.*[53] also presented correlation between the d-band centre and the TOF in the DRM reaction in Ni–M alloys (M = Fe, Co, Cu). Conversely, the TOF became lower when the d-band centre was closer to the Fermi level. Therefore, the d-band centre of the metal surface is generally reliable as a descriptor to predict the activation barrier of methane dissociative adsorption, but one must consider the possibility of an optimum value of the d-band centre or the possibility that the d-band centre alone cannot explain the behaviour.

3. Coke formation mechanism

As described above, carbon deposition on Ni catalysts is a major issue in SRM and DRM. To overcome this difficulty, understanding the coke formation mechanism is important. In this chapter, the mechanism of carbon deposition is summarized.[17,54–57] Also, methods to suppress carbon deposition by alloying and other methods are described.

3.1 Formation of adsorbed C species

Formation of the C species, which engenders coke formation, occurs as side reactions such as the methane decomposition reaction (eqn (6)) and the Boudouard reaction (eqn (7)).

$$CH_4 \rightarrow C + 2H_2 \quad \Delta H^0_{298} = +75 \text{ kJ mol}^{-1} \tag{6}$$

$$2CO \rightarrow C + CO_2 \quad \Delta H^0_{298} = -171 \text{ kJ mol}^{-1} \tag{7}$$

Whether the formation of a carbon species occurs or not is determined by the thermodynamic balance between the main reaction and the carbon deposition side reaction.[58,59] Fig. 2 presents the limit of carbon formation from CH_4 at 25.5 atm. The left side of the central curve shows the H/C and O/C ratios at which there is potential for carbon deposition. As shown in Fig. 2, the larger the ratio of H or O to C is, the more difficult it is for carbon to form. For this reason, SRM processes are operated industrially under conditions with a

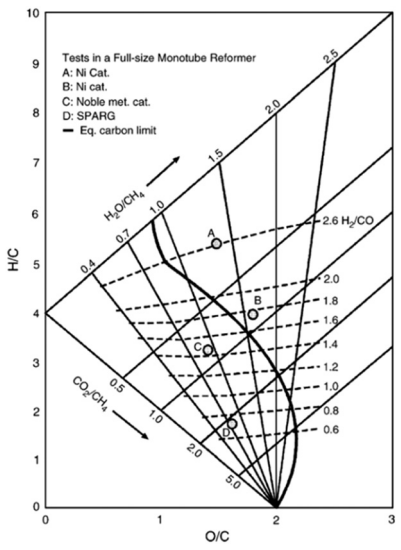

Fig. 2 The diagram of carbon limit. The left side of the bold curve has the potential for carbon deposition. Reprinted with permission from ref. 58. Copyright 2006 Elsevier.

great amount of steam, such as steam to CH_4 ratios of 2.5–3.0,[21] requiring much energy to supply the excess steam. In addition, Yoon *et al.*[60] recently reported the necessity of considering not only the CH_4 decomposition steps (steps 1–4) but also the CO gasification steps (steps 5–7) when considering the C species formation (Fig. 3). In these steps, step 4 or step 5 are alternatives. If steps 5–7 occur after step 3, then carbon deposition could be suppressed by CO gas production.

$$\text{Step 1}: CH_4^* \rightarrow CH_3^* + H^*$$

$$\text{Step 2}: CH_3^* \rightarrow CH_2^* + H^*$$

$$\text{Step 3}: CH_2^* \rightarrow CH^* + H^*$$

$$\text{Step 4}: CH^* \rightarrow C^* + H^*$$

$$\text{Step 5}: CH^* + O^* \rightarrow CHO^*$$

$$\text{Step 6}: CHO^* \rightarrow CO^* + H^*$$

$$\text{Step 7}: CO^* \rightarrow CO(g)$$

They investigated the pathway of SRM on the Ni(111) surface and Ni-Ru and Ni-Rh alloy surfaces using DFT calculations and MD (molecular dynamics). First, the adsorption energy of CH_4 on Ni is very weak (approx. −0.02 eV), indicating that CH_4 molecules are physisorbed. Next, the C–H bond of CH_4 is broken and CH_4 decomposition proceeds to form CH* species (steps 1–3). Furthermore, two paths exist: one where CH* decomposes into C* and H* (step 4), and another where CH* reacts with O* to form CHO* (steps 5–7). Because the activation barrier of the former path (CH* → C* + H*) is high, the latter path (CH* + O* → CHO*) occurs more preferentially irrespective of Ni surfaces or Ni alloy surfaces. The activation barrier of Ru-doped Ni surface for step 5 was the smallest, which suggests that Ni-Ru has the lowest activation energy and that it is the most effective at suppressing carbon deposition.

In addition, the stability of the C atom on the metal surface is often discussed to explain whether the catalysts are prone to coke formation. Besenbacher *et al.*[61] investigated the stability of the C atom on Au/Ni(111) by DFT calculation, which revealed that the C atoms were less stable on a Au-loaded Ni surface. Lower stability of the adsorbed C atoms on the metal leads to a greater likelihood that they will react with the adsorbed O species to produce CO, thereby suppressing the nucleation of graphite. Consequently, the stability of C atoms on alloy surfaces is expected to be an indicator of the ease of carbon deposition. Relevant details are presented in section 4.1.

3.2 Growth of C species making coke

Carbon atoms (C_α) bind other C species on the Ni metal to form larger carbon species.[54,62,63] Fig. 4 and Table 2 summarize coke formation of various types. The adsorbed atomic carbon (C_α) forms C–C bonds on the surface and rearranges to form polymeric amorphous carbon (C_β), which is less reactive than C_α. C_β species accumulate on the Ni surface, thereby forming graphite platelet films (C_c), or dissolve into Ni bulk. For reactions of heavy hydrocarbon, encapsulating carbons that cover Ni are sometimes produced. Then Ni carbide, Ni_3C, is formed in the bulk (C_γ). Vermicular carbon or whiskers (C_v) are formed by the solid solution of C species in Ni metal. Whisker carbon is formed when C species formed on the Ni surface dissolve into the Ni metal, diffusing, and pushing up Ni particles from the opposite side (Fig. 4). Formation of numerous whisker carbons is expected to engender the destruction of the catalyst itself. The encapsulating carbons covering the Ni surface lead to decreased activity.

Factors such as the Ni ensemble size and particle size also play important roles in the growth of C species. Rostrup-Nielsen[17] reported the numbers of Ni metal ensembles required for each process (eqn (8)). In eqn (8), subscript letters n, m, m', respectively represent the numbers of Ni

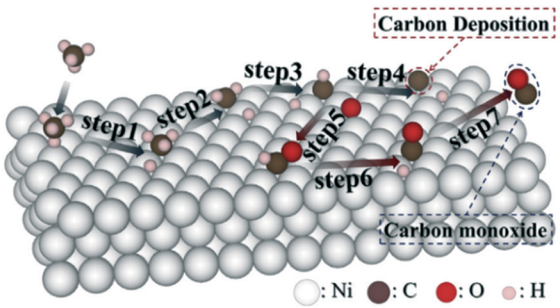

Fig. 3 The schematic images of reaction paths for SRM on Ni. Reprinted with permission from ref. 60. Copyright 2017 Elsevier.

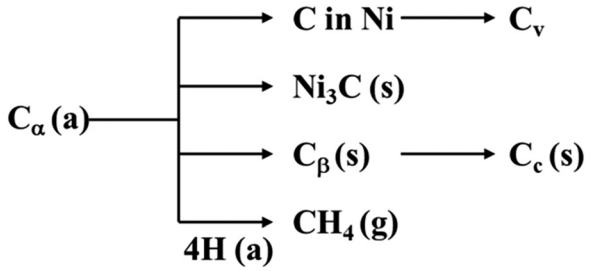

Fig. 4 Formation, gasification, and transformation of carbon on nickel form carbon monoxide (a, g, s refer to adsorbed, gaseous, and solid states, respectively). Reprinted with permission from ref. 63, redrawn. Copyright 1982 Marcel Dekker Inc. Taylor & Francis ltd, https://www.tandfonline.com.

Table 2 The various structures of carbon formation. Reprinted with permission from ref. 63. Copyright 1982 Marcel Dekker Inc. Taylor & Francis ltd, https://www.tandfonline.com

Structural type	Designation	Temperature/K
Adsorbed, atomic carbon (surface carbide)	C_α	473–673
Polymers, amorphous films, or filaments	C_β	523–773
Graphite (crystalline) platelet, films	C_c	773–823
Vermicular (polymeric, amorphous) filaments or whiskers	C_v	573–1273
Ni carbide (bulk), Ni_3C	C_γ	423–523

atoms required for CH_4 dissociation, C species formation, and dissolution of C species into Ni metal. Although Ni ensembles are also required for CH_4 dissociation, the necessary numbers for CH_4 activation and formation of C species are smaller than that required for C species to dissolve into Ni ($m' > n$, m). In addition, Rostrup-Nielsen[17] described in that report that three Ni atoms are involved in the CH_4 reforming reaction.

$$CH_4 \rightarrow CH_{x-}{}^*{}_n \rightarrow C_-{}^*{}_m \rightarrow C_-{}^*{}_{m'} \rightarrow Ni, C \rightarrow C\text{-Whisker} \quad (8)$$

Furthermore, some papers have reported the Ni particle size effect on carbon. Kim *et al.*[64] reported that carbon deposition is likely to occur when the Ni particles are larger than 7 nm. Vogt *et al.*[47] reported that the maximum amount of surface carbon deposition was found at about 4 nm for SRM, and reported the amount of carbon increased with nanoparticle size for DRM. The low-coordinated Ni sites can be sites of carbon nucleation.[65,66] Therefore, considering the coke formation mechanism described above, coke formation can be suppressed by loading small metal particles, by alloying the supported metal, by diluting the ensemble of active metals necessary for the dissolution-precipitation nucleation of carbon whiskers, or by blocking the low-coordinated sites which can be carbon nucleation sites.

4. Effects of alloying on steam reforming of methane (SRM)

This chapter summarizes effects of alloys on activity, selectivity, and durability in SRM. Industrially, Ni catalysts supported on Al_2O_3 are used widely.[21,39] Noble metal catalysts (Rh, Ru, Pd, Pt, *etc.*) are highly active and stable, but they are too expensive for industrial use. Ni is cheap and common, but it presents difficulties such as catalyst deactivation

Table 3 The effect of Ni-based alloy for SRM

	Properties of metal		Catalytic performance			Resistance			
	Metal reductivity	Metal dispersion	Activity	Selectivity	Long-term stability	Coke	Sulphur	Sintering	Remarks
Fe–Ni	High		High		High	High	High		Fe could enhance the resistance for sulphur
Co–Ni		Low	Low		High				Co block the low-coordinated Ni sites
Cu–Ni	High		High	High WGS sel.		High			Cu could promote WGS
Sn–Ni			Low		High	High			Sn increases the apparent activation energy
Ru–Ni	High		High		High	High			Not need the H_2-treatment before activity tests
Rh–Ni	High	High	High	Low WGS sel.	High			High	Rh–Ni has self-activation and self-regenerative activity
Ag–Ni			Low		High	High			Ag blocks the more active sites such as steps and edges The apparent activation energy increases by Ag addition
Re–Ni	High		High	Low WGS sel.	High				Re addition does not enhance WGS Re–Ni has higher TOF than Ni
Ir–Ni	High	High	High			High		High	Ir addition could enhance the sintering resistance Ir increases the barrier for CH_4 dissociation
Pt–Ni	High	High	High		High	High			A small amount of Pt increases the metal dispersion, but excessive amounts of Pt lead to agglomeration Pt increases the activation barrier for CH_4 dissociation
Au–Ni	High		High/low		High	High	High		A barrier for CH_4 dissociation increases by Au addition. C atom is less stable on Au/Ni surface

because of carbon deposition, sintering, and poisoning, and lower activity than that of noble metals. Therefore, the development of catalysts with high activity and high durability is required. Many studies have examined catalysts using Ni alloyed not only with base metals, but also with noble metals.

Table 3 briefly presents the catalytic performance of the Ni-based catalysts supported on oxide supports introduced in this chapter. The respective sections provide relevant details. This table, which roughly categorizes the properties of metal, catalytic performance, and stability, presents the superiority or inferiority of each item compared to a single Ni catalyst. Blank spaces indicate that the corresponding survey has not been conducted. It is noteworthy that the alloy effects often vary depending on the catalyst, composition, oxide support, reaction conditions, *etc.* This table shows only representative features.

Some alloy catalysts reportedly have not only resistance to carbon deposition but also to sulphur and sintering, thereby providing improved long-term stability compared to Ni catalysts. In many alloys, negative effects such as an increase in the CH_4 dissociation barrier have also been reported. In some cases, total activity was improved because of the effects of improved metal reducibility or dispersibility by addition of the second metal. In still other cases, WGS selectivity (CO selectivity) was reported as changed by the alloying.

4.1 Addition of base metal to Ni catalysts

The addition of base metals to Ni presents many benefits, including improved coke resistance, increased sulphur resistance, and improved reducibility and dispersibility of Ni, although the catalyst component is still inexpensive. However, some secondary metals reduce the initial activity slightly. Therefore, it will be necessary to control selection of the secondary metal and the composition ratio carefully.

Fe–Ni. Various structures such as core–shell, supported, and reductive precipitation of perovskite oxides have been reported for Ni catalysts doped with Fe. In addition, high activity, high resistance to carbon deposition, resistance to sulphur poisoning, and improved Ni reducibility have been reported. Tsodikov *et al.*[67] reported that the core–shell catalysts with a Ni–Fe alloy nanoparticle core and a γ-Fe_2O_3 shell showed high activity for SRM and stability to coke formation and resistance to H_2S (Fig. 5). The catalyst was produced by H_2 reduction of Ni-loaded spinel $Mg(FeAl)_2O_4$ support. Its structure was characterized using XRD, XAFS, HRTEM, and Fe Mössbauer data. The reaction tests confirmed the core–shell structure: the core was a metallic NiFe alloy cluster; the shell was superparamagnetic γ-Fe_2O_3. They described that NiFe alloy provides high activity comparable to the commercial catalyst, and that the γ-Fe_2O_3 shell was the active site for the decomposition of H_2S to S. Konstantinov *et al.*[68] reported that Ni-Fe alloy catalysts prepared by epitaxial coating on the commercial spherical γ-Al_2O_3 showed high activity for SRM and showed resistance

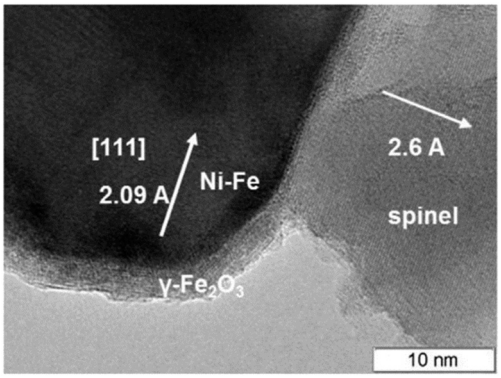

Fig. 5 TEM images of Ni-loaded spinel $Mg(FeAl)_2O_4$ after reaction tests. The core–shell structure was observed; core is Ni–Fe alloy, shell is γ-Al_2O_3. Reprinted with permission from ref. 67. Copyright 2015 Elsevier.

to H_2S. Activity tests over Ni–Fe alloy catalysts and commercial SRM catalyst (NIAP 03-01) were conducted for 30 h with 30 ppm H_2S. Although the activity of commercial NIAP 03–01 decreased after 10 h because of the H_2S poisoning, that of Ni–Fe alloy catalyst remained high for 30 h. They assumed that the conversion of H_2S to S occurred during the reaction. Subsequent XRD, TEM, and Mössbauer spectroscopy of Fe revealed that the catalyst after the activity tests contained $MgFe_{0.1}Al_{1.9}O_4$ spinel phase, metallic Ni, γ-FeNi, and $FeAl_2O_4$ iron–aluminium spinel, but not sulphur-containing compounds. They inferred that both high SRM activity and decomposition of H_2S to S occurred because Ni–Fe alloy particles bonded tightly to the support.

Djaidja *et al.*[69] also reported the increased coke resistance of Ni–M/MgO or $(Ni–M–Mg)_2Al$ (M = Fe, Cu). Their results showed that Ni–Fe or Ni–Cu alloying improves Ni reducibility, high activity, and high carbon tolerance. Furthermore, Provendier *et al.*[70] and Thalinger *et al.*[71] reported effects of Fe on Ni–perovskite supports. Provendier *et al.*[70] investigated the series of $LaNi_xFe_{1-x}O_3$ ($0 \le x \le 1$) and found that although the no NiFe alloy was formed, the addition of Fe to perovskite supports can decrease the Ni particle size, thereby limiting coke formation. Thalinger *et al.*[71] investigated two Ni–perovskite catalysts; Ni–$La_{0.6}Sr_{0.4}$-$FeO_{3-\delta}$ (lanthanum strontium ferrite, LSF) and Ni–$SrTi_{0.7}Fe_{0.3}$-$O_{3-\delta}$ (strontium titanium ferrite, STF). Ni–Fe alloy particles were observed after H_2 treatment. These manifestations depend on the reducibility of supports. They described that, because LSF has more reducibility than STF, the degree of Ni–Fe alloying is high, resulting in suppressed catalytic performance. Consequently, optimization of the complex oxide support and the reduction conditions can lead to control of the supported Ni–Fe catalysts.

Co–Ni. You *et al.*[65] reported the role of Co addition to Ni/Al_2O_3 catalysts. After Ni–Co/Al_2O_3 catalysts with 1–15%Co and 12%Ni were prepared using the co-impregnation method, their activity and stability toward coke were investigated. In fact, Co addition leads to decreased metal dispersion, and thereby activity at low temperature. However, 180 h stability

tests conducted at 1073 K revealed that 7%Co–12%Ni/Al_2O_3 catalysts retained high activity of 95% for 180 h, although 12%Ni showed deactivation. Their results show that Co can block the active low coordinated Ni sites and that it can increase coke resistance.

Cu–Ni. Reportedly, Ni–Cu alloying provides benefits such as improved Ni reducibility, high activity, high carbon tolerance, and high WGS activity.

As described in the Fe–Ni section, Djaidja *et al.*[69] investigated the increased coke resistance of Ni–M/MgO or $(Ni–M–Mg)_2Al$ (M = Fe, Cu). Results showed that Ni–Fe or Ni–Cu alloying offers improved Ni reducibility, high activity, and high carbon tolerance. Huang *et al.*[72] reported that the effect of Cu addition to Ni supported on Sm-doped ceria, Gd-doped ceria, and α-Al_2O_3. Activity tests over 2wt%Ni catalysts showed that Ni catalyst supported by Sm-doped ceria had much higher activity at a lower temperature, the highest H_2 production rate, and the lowest carbon formation rate. This markedly increased activity was driven by the high surface area and oxygen-ion conductivity of the doped ceria support. Next, a series of Ni–Cu catalysts supported on Sm-doped ceria support was prepared by the co-impregnation method and was examined its catalytic properties. Although Cu is inactive for SRM, 0.1wt%Cu–0.5wtNi catalyst showed a much higher CH_4 conversion rate and higher H_2 production rate than the 0.5wt%Ni catalyst. Because Cu catalyst is well known to show high WGS activity, the addition of Cu can increase the WGS activity and therefore SRM activity by increasing the CO removal rate.

Sn–Ni. Nikolla *et al.*[66,73] reported that the addition of Sn to Ni catalyst can improve long-term stability, although the initial activity is slightly lower than that of Ni catalyst. 1wt%Sn or 5 wt%Sn was loaded on Ni/YSZ by the incipient wetness method. Fig. 6 presents results of long-term stability tests over these catalysts. As shown in Fig. 6, the addition of 1wt%Sn can drastically increase the stability, although 5 wt% of Sn led to decreased activity. In addition, the apparent activation barriers they calculated were 101 ± 4 kJ mol^{-1} for Ni, and 132 ± 4 for 1wt%Sn/Ni supported on YSZ.[66] Moreover, DFT calculation revealed that Sn atoms preferentially displace low-coordinate Ni sites. Consequently, the main active sites were moved from under-coordinated Ni sites, where carbon nucleation occurs, to more abundant well-coordinated Ni sites. Amounts to Ni catalysts. Their effects on carbon deposition are mainly reported.

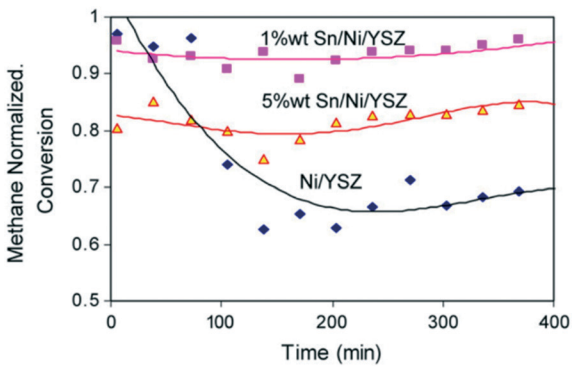

Fig. 6 The long-term activity of Ni/YSZ, 1wt%Sn/Ni/YSZ, 5 wt%Sn/Ni/YSZ measured at the steam/carbon ratio of 0.5 and at 1073 K. the 1 wt% addition of Sn could improve the stability with a little of decrease in initial activity. Reprinted with permission from ref. 73. Copyright 2007 Elsevier.

4.2 Addition of noble metals to Ni catalysts

The addition of noble metals to Ni catalysts in small quantities has attracted much attention in recent years. In many cases, small amount of noble metals (Ru, Rh, Ag, Pt, Au, *etc.*) are added to Ni catalysts. Their effects on carbon deposition are mainly reported.

Ru–Ni. Nawfal *et al.*[74] investigated SRM activity using catalysts impregnated with 0.5wt%Ru supported on Ni_xMg_{6-x}-Al_2 oxide prepared by a hydrotalcite route. Among these catalysts, 0.5wt%Ru/$Ni_6Al_2O_x$ showed the highest activity. They required no reduction treatment before reactions. In fact, 0.5wt%Ru/$Ni_6Al_2O_x$ remained highly active after 10 cycles of tests. The surface carbon did not decrease the activity. The Ru–Ni interaction was sufficient to show that Mg was not necessary for the oxide. In addition, as described in chapter 3, Yoon *et al.*[60] calculated the activation energies of each step involving the CO gas evolution and predicted that the addition of Ru to alloy is effective for suppressing carbon deposition. Baek *et al.*[75] reported that Ru/Ni/$MgAl_2O_4$ has self-activation property and that H_2 treatment was not necessary.

Rh–Ni. The introduction of a small amount of Rh on Ni catalyst has been studied. Some benefits have been reported such as improved activity, high H_2 yield, resistance to sintering, self-activation, and self-regenerative activity.

Katheria *et al.*[76] investigated the effects of small amounts of Rh doped to Ni catalysts. First, *x*wt%Rh–15 wt%/$MgAl_2O_4$ (x = 0.1–1.0) were prepared using the sequential impregnation method. Activity tests over these catalysts were conducted under ambient and high-pressure conditions (Fig. 7). Activity tests at ambient pressure showed that a small amount of Rh (0.1wt%Rh) was able to increase the SRM activity and H_2 yield drastically, but a further increase of Rh amount did not engender a further increase of activity or H_2 yield. However, activity tests conducted at high pressures over these catalysts differed. The degrees of stability over 0.5wt%Rh and 1.0 wt%Rh loaded catalysts were similar but those over 0.1wt%Rh or 0wt%Rh loaded catalysts were lower. In addition, the CO selectivity of Rh–Ni catalysts was higher than that of Ni catalysts at both pressures. The presence of Rh on the surface and the smaller crystallite size of active metals by the addition of noble metal might be attributed to the higher CO selectivity.

Morales-Cano *et al.*[77] reported that Ir or Rh addition to Ni catalysts can suppress sintering. After they prepared 2.89wt%Ni/Al_2O_3, 0.97wt%Ir–2.91wt%Ni/Al_2O_3, and

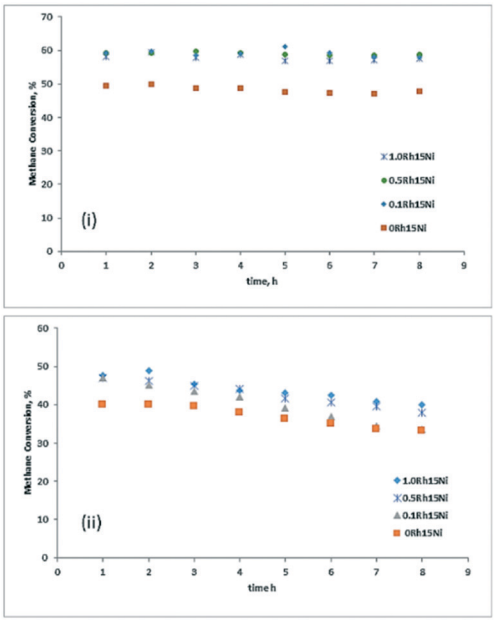

Fig. 7 The effect of Rh loading amount on methane conversion at pressure (i) 1 bar and (ii) 10 bar at 873 K; GHSV, 2.0×10^6 h^{-1}; *W*/*F* is 0.34 g_{cat} h mol^{-1}. Reprinted with permission from ref. 76. Copyright 2019 Elsevier.

1.12wt%Rh–2.92wt%Ni/Al_2O_3 by incipient wetness impregnation, aging treatments were conducted at 1073 K, under 30 bar, and H_2O/H_2 atmospheres for 240 h to simulate long-term stability. After the aging process, Ni particles of Ni/Al_2O_3 were larger than 100 nm, whereas Ni–Ir/Al_2O_3 and Ni–Rh/Al_2O_3 particles were smaller than 50 nm.

In addition, Li *et al.*[78] reported that the Rh-doped MgAlO oxide has self-activation and self-regenerative activity, although Ru-doped MgAlO does not. These activities were achieved by the oxidative incorporation of surface NiO into the lattice Ni^{2+} of Mg(Al, Ni)O and the reductive transfer of lattice Ni^{2+} to surface Ni^0 by hydrogen spill over, leading to continuous regeneration of active Ni metal particles.

Ag–Ni. Effects of the addition of Ag to Ni catalyst have been reported by Dam *et al.*[79] and Wang *et al.*[80] According to DFT calculations,[80] Ag selectively substitutes for the more active sites of Ni, such as edges and steps. In the Ni–Ag alloy system, Ag is inactive to SRM. Moreover, the addition of Ag reduced the activity of adjacent Ni sites significantly because of charge donation from Ag to Ni. Fig. 8 portrays Arrhenius plots of Ni, $Ni_{0.95}Ag_{0.05}$, and $Ni_{0.75}Ag_{0.25}$ supported on $MgAl_2O_4$. The apparent activation energies of these catalysts were calculated respectively as 103.6 kJ mol^{-1} for Ni, 119.5 kJ mol^{-1} for $Ni_{0.95}Ag_{0.05}$, and 127.3 kJ mol^{-1} for $Ni_{0.75}Ag_{0.25}$. Consequently, Ag addition to Ni catalyst engenders decreased SRM activity, decreased TOF, and increased apparent activation energy.[80] However, Ag can increase the carbon resistance by blocking the active sites on the steps for the nucleation and growth of the filamentous carbon.[79] Dam *et al.*[79] reported that only 3wt%Ag replaced with Ni led to a carbon amount that was

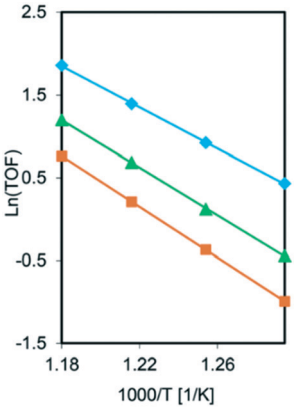

Fig. 8 The Arrhenius plots for 12wt%Ni (◆, blue), 12wt%$Ni_{0.95}Ag_{0.05}$ (▲, green) 12wt%$Ni_{0.75}Ag_{0.25}$ (■, orange). Reaction conditions: S/C = 3.5, CH_4/H_2 = 10, W/F_0 between 0.018 and 0.037 g s mol^{-1}. Reprinted with permission from ref. 80. Copyright 2017 RSC publishing.

one order of magnitude lower, thereby suppressing the formation of filamentous carbon.

Re–Ni. Xu *et al.*[81] and Wang[82] reported the superiority of Ni–Re alloy catalysts. Xu *et al.*[81] reported the enhancement of catalytic activity and stability by adding Re to Ni monolithic catalysts. They loaded 5 wt%Ni and 0.5, 5, and 10 wt%Re directly on Ni monoliths without oxide support and designated them respectively as Ni_5, $Ni_5Re_{0.5}$, Ni_5Re_5, and Ni_5Re_{10}. Fig. 9 shows the turnover frequency (TOF), defined as the number of H_2 molecules formed per second per Ni active site, were calculated and shown. These results demonstrated that the increment of Re amount can enhance both the catalytic activity and stability. Furthermore, CO selectivity increased for Ni–Re alloy catalysts compared to Ni, suggesting that the addition of Re promoted the SRM reaction, but not the WGS reaction. XRD, *in situ* X-ray absorption fine structure spectroscopy (XAFS) during H_2 reduction, and H_2-TPR revealed that Re can drastically promote the reduction of NiO to Ni. Moreover, DFT calculations revealed that the adsorption energy of a hydrogen atom on Re(001) was smaller than that on Ni(111), Ni(011), and Ni(001).

Therefore, the H atom adsorbed more readily onto Re than on Ni during the reaction, thereby preventing oxidation of the surrounding Ni and enhancing the stability. Wang also

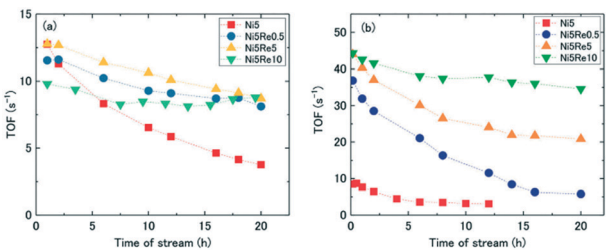

Fig. 9 TOFs as a function of TOS at (a) 873 K (b) 973 K. $CH_4/H_2O/N_2$ = 10/13.6/30 mL min^{-1}, GHSV = 6400 h^{-1}. Reprinted with permission from ref. 81. Copyright 2020 RSC publishing.

reported Ni–Re alloy nanowire type catalysts, which showed low-temperature activity at 623 K.[82]

Ir–Ni. As described in the Rh–Ni section, Morales-Cano *et al.*[77] reported that Ir or Rh addition to Ni catalysts can suppress sintering. Furthermore, Liu *et al.*[83] reported increased coke resistance and dispersibility of metal particles over Ir doping to $Ni/MgAl_2O_4$ on bi-reforming of CH_4 with steam and CO_2. The formation of Ir–Ni alloy was confirmed after H_2 treatment by HAADF-STM. The metal particles of $Ir_{10}Ni_{90}/MgAl_2O_4$ were 2–3 nm, although those of $Ni/MgAl_2O_4$ were 5–40 nm. Because nucleation of carbon occurs on large ensembles, coke formation occurs only with difficulty on such small metal particles. Furthermore, XPS measurements revealed that more C–O species were formed on $Ir_{10}Ni_{90}/MgAl_2O_4$ than in $Ni/MgAl_2O_4$, indicating that the addition of Ir promoted the oxophilicity of the metal surface. The increased amount of surface oxygenates was inferred as the reason for the increase in coke gasification rate during the catalytic process. Although Ir doping increased the apparent activation energy, it increased the coke resistance because of the small ensemble sizes, increased oxophilicity, and increased the barrier for CH_4 dissociation.

Pt–Ni. Jaiswar *et al.*[84] reported the effects of a small amount of Pt doping to $Ni/MgAl_2O_4$. They prepared the Pt doped 15wt%Ni catalysts supported on $MgAl_2O_4$ by the sequential impregnation method, varying Pt loading amount from 0.01–1.0 wt%. The prepared catalysts, *x*w%Pt–15w%Ni/$MgAl_2O_4$ were denoted as *x*Pt15Ni. Three effects of Pt doping can occur: increased reduction of the supported metal, increased dispersion, and increased SRM activity. First, it was confirmed using H_2-TPR measurements that, as Pt amount increased, the degree of reduction increased. The degree of reduction of 0Pt15Ni was 44.9%, but that of 1.0Pt15Ni was 67.7%. In addition, the average particle sizes of supported metals estimated from TEM images decreased by the addition of Pt. The average sizes of 0Pt15Ni, 0.1Pt15Ni, and 1.0Pt15Ni were, respectively, 14.9 nm, 7.6 nm, and 9.3 nm. Those sizes indicate that a small amount of Pt can increase the dispersibility of metal, but an excessive amount of Pt addition engenders agglomeration. Furthermore, activity tests over these prepared catalysts at 873 K at 1 or 10 bar pressures revealed that Pt doping amount of up to 0.1 wt% can increase the SRM activity, but a further increase of Pt led to the decrease of SRM activity. The activity was stable for 8 h over all catalysts during tests at 1 bar, but they decreased gradually during tests at 10 bar. Among the catalysts, 0.1Pt15Ni showed the highest activity and the latest rate of deactivation. The authors concluded that the high SRM activity of 0.1Pt15Ni corresponds to the high surface area of metal, and that stability corresponds to the small metal size because earlier reports show that the low particle size of the metal decreases the carbon formation rate.[85]

Related to this research, the effect of Pt doping to Ni catalysts or Pt–Ni alloy for CH_4 dissociative chemisorption, the rate-determining step of SRM, has been studied using DFT calculation by Roy *et al.*[42] As described herein, activation energies for CH_4 dissociative chemisorption on Pt-doped Ni-based alloy and Ni-doped Pt-based alloy surface were calculated from transition-state calculations. In the case of Ni-based alloy, the activation barrier increased linearly with the amount of Pt. However, no linear increase or decrease trend was observed for Ni-doped Pt-based alloy. DFT calculation also demonstrates the relation between the activation energy and the d-band centre; the activation energy decreased as the values of the d-band centre increased. However, they also described that a single surface-based descriptor cannot provide a complete understanding of the reactivity changes.

Au–Ni. Details of Au–Ni alloys have been investigated by Besenbacher *et al.*[61] using techniques such as STM and DFT calculation to study their effects on CH_4 activation and carbon deposition. Some alloys do not mix in bulk but instead form stable alloys on the outermost surface: Au–Ni is of this type. In Fig. 10 (left), the black circles represent Au. The Ni around the Au has a different colour from that of normal Ni, signifying different electronic density of states. The DFT calculation shows that one neighbouring Au increases the barrier to CH_4 dissociation on Ni atoms by 16 kJ mol^{-1}, whereas two neighbouring Au atoms increase it by more than a factor of two. The dissociation on Au atoms is expected to have a higher barrier. The Au–Ni alloy effects on carbon deposition are also described in terms of the stability and coverage of C atoms adsorbed onto the Ni surface. Lower stability of the adsorbed C presents a stronger tendency to react with adsorbed O to form CO, and to give lower coverage of the C atoms. The energies of C atoms on the Ni(111) and Au/Ni(111) surfaces were calculated using DFT calculation (Fig. 10(right)). The stability of the C species at the Ni site next to Au is reduced considerably.

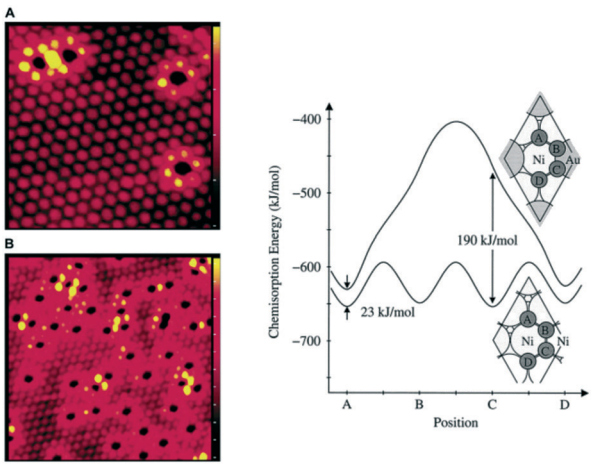

Fig. 10 (left) the STM images of Ni(111) with (A) 2% and (B) 7% of a Au monolayer. The Ni atoms adjacent to Au looks brighter than normal Ni, indicating the different electronic states. (Right) The calculated chemisorption energy of C atom on the different positions A–D of Ni(111) or Au/Ni(111) by DFT calculation. The presence of Au significantly increases the chemisorption energy of C atom. Reprinted with permission from ref. 61. Copyright 1998 AAAS.

Rocha *et al.*[48] also reported effects of Au addition to Ni/Al_2O_3 catalysts. The Au–Ni catalysts were prepared by mixing the Au solution with the reduced Ni/Al_2O_3. Diffuse reflectance infrared Fourier transform spectroscopy of adsorbed CO (DRIFTS-CO) revealed that the Au atoms blocked the low-coordinated Ni sites, such as steps and corners, and modified the Ni surface structure. In addition, by adding Au, the CO adsorption form changed from a bridge to a linear form. The electronic density was increased by the electron transfer from Au to Ni. Activity tests revealed that the addition of Au to Ni catalysts engenders a decrease the SRM activity. The authors conclude that blocking of the low coordinated Ni sites by Au, the decreased stability of intermediaries engender hindrance of the growth of graphitic carbon.

Palma *et al.*[86] investigated effects of Au addition to $NiLaO_3$ perovskite support and described that Au substitutes the step sites of Ni and suppresses carbon deposition. Although Au–Ni has a negative effect on CH_4 activation because the Ni step sites are also active sites for C–H activation and because Au decreases the activity of surrounding Ni atoms, the total activity is enhanced because of increased Ni dispersion by Au addition. Chin *et al.*[87] also reported decreased initial activity and deactivation rate. Sapountzi *et al.*[88] reported that Au-modified Ni catalyst showed sulphur resistance and increased reducibility of NiO. In addition, Wang *et al.*[89] used STM and DFT calculations to investigate single-atom alloys of Ni on the Au(111) surface. They described that Ni–Au can improve the surface activity of Au(111) considerably because of the high CO adsorption of Ni atom on Au(111). Therefore, Au–Ni catalysts might be catalysts with high stability, although they reduce the initial activity slightly.

4.3 Others

Co-based alloy catalyst. Shen *et al.*[90] investigated single and bimetallic Co-based catalysts (Co, Co–Ni, Co–Cu, Co–Al) supported on CeO_2. Among Co/CeO_2 catalysts with different Co loading amounts, 12%Co/CeO_2 showed the highest CH_4 conversion. The Co–Ni and Co–Al catalysts showed superior activity to that of Co single catalysts. However, the H_2 yield of Co–Al was much lower. The highest level of performance was exhibited by $Co_{80}Ni_{20}$ (total weight 16 wt%) catalysts.

Pd–Zn catalysts in an electric field. The author's group investigated SRM in an electric field.[91–95] In this system, constant current is applied after two electrodes are inserted on and under the catalyst bed (Fig. 11(Left)). Manabe *et al.*[91] and Okada *et al.*[92] revealed that the reaction mechanism in an electric field differs from that of a conventional thermal catalytic reaction. In an electric field, the proton conduction on oxide supports occurs; then CH_4 dissociative adsorption occurs because of collision of the proton. Results demonstrated further that the active sites for SRM in an electric field differ. The active sites for thermal catalysis are metals on the surface, but those in an electric field are metals at the perimeter.

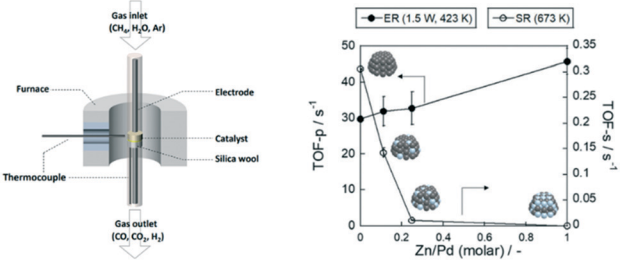

Fig. 11 (Left) The schematic images of the reactor. Two electrodes are inserted on and under the catalyst bed and the electrical current was applied. (Right) The calculated TOFs of PdZn/CZO with Zn/Pd ratios for thermal catalysis, SR, (○) and catalysis with an electric field, ER (●). Reaction conditions: $CH_4/H_2O/Ar$ = 1/2/7, total flow rate = 100 sccm; catalysts weight, 100 mg; furnace temperature, 423 K for catalysis with an electric field, 673 K for thermal catalysis; input power 1.5 W. reprinted with permission from ref. 96. Copyright 2020 RSC publishing.

The author of this review investigated effects of Pd–Zn alloy on catalytic activity for SRM in an electric field.[96] A series of Pd–Zn alloys with different composition ratios (Zn/Pd = 1/9, 1/4, 1/1, molar ratios) and fixed Pd loading weight (5 wt%) loaded on $Ce_{0.5}Zr_{0.5}O_2$ were prepared and tested. Calculation of TOF over these catalysts revealed the different effects of Zn addition on TOFs with or without an electric field (Fig. 11(right)). In Fig. 11(right), TOF normalized by the number of metal atoms on the surface (TOF-s) was used for the thermal SRM and TOF normalized by the number of metal atoms at the perimeter was used for the SRM in an electric field based on the different reaction mechanisms. In the case of the normal thermal catalytic reaction, the TOF decreased concomitantly with increasing Zn content; Pd1Zn1 was almost inactive. This finding might be attributable to dilution of the Pd–Pd ensemble by Zn addition. It is noteworthy that Pd1Zn1, which was almost inactive in the thermal catalytic reaction, showed the highest TOF value in the electric field. This might indicate that ensembles of metals are no longer necessary for the reaction in the electric field. Furthermore, from the CO adsorption IR, the ligand effect was observed that the electron density of Pd increased concomitantly with increasing Zn addition. The intermediate of SRM in the electric field is regarded as cationic. The cationic intermediate might be more stable on electron-enriched Pd. Consequently, the effects of alloys for catalysis in the electric field differ greatly from those of thermal catalysis.

5. Effects of alloying on dry reforming of methane (DRM)

Because DRM is an attractive process that can convert the greenhouse gases of methane and CO_2 into useful chemicals (CO and H_2), numerous studies of DRM have been conducted to date. Widely various alloy catalysts have been investigated. Yentekakis *et al.*,[25] Bian *et al.*,[26] and Aziz *et al.*[27] have provided comprehensive summaries of alloys in DRM.

Therefore, this chapter introduces recent studies of alloy DRMs published over the last five years.

Alloy catalyst structures of several types have been introduced in this chapter. Some are metal-supported on Al_2O_3 or other supports, others are core–shell catalysts with alloy nanoparticles encased in oxides, whereas others investigated widely in recent years are alloy metal particles formed by hydrogen reduction of oxide precursors that include Ni and secondary metals in their composition. Table 4 briefly summarizes the catalytic performance of Ni-based catalysts supported on oxide supports introduced in this chapter. The dedicated sections provide relevant details for them. This table roughly categorizes the properties of metal, catalytic performance, and stability, and presents the superiority or inferiority of each item compared to a single Ni catalyst. Blank spaces show that the corresponding survey has not been conducted. It is noteworthy that the alloy effects often vary depending on the catalyst, composition, oxide supports, reaction conditions, *etc.* This table presents only representative features.

Many catalysts show higher coke resistance than that of Ni, with enhanced long-term stability by blocking the more active sites of Ni, such as edge sites or step sites. This feature also reduces the activation of methane, but in some alloy catalysts, it has also been noted that the total activity can be increased because of the effects of improved metal reducibility and dispersibility. In addition, some ternary catalysts reportedly show better catalytic performance than bimetallic catalysts show. It is expected that more good catalysts will be reported as research progresses. For details, please refer to 5.3, "others".

5.1 Addition of the base metal to Ni catalysts

The addition of transition metals to Ni catalysts often changes activity and stability depending on the amount added. For example, Ni–Cu shows high activity and durability at the optimum Cu/Ni ratio, but carbon deposition tends to occur at higher or lower ratios. It is necessary to add an optimal amount of a second metal because it can not only enhance stability. It can also decrease the CH_4 activity drastically.

Mn–Ni. Recently, Najfach *et al.*,[97] and Ramezani *et al.*[98] reported effects of Mn to Ni catalysts. They described effects of increased Ni dispersibility, which led to less coke formation. Ramezani *et al.*[98] described that the Mn could increase the activity because of the higher dispersion of Ni and concluded that 10 wt%Ni–3wt%Mn/Al_2O_3 is the optimal catalyst, showing long-term stability for 20 h. Najfach *et al.*[97] investigated Mn–Ni catalysts on various zeolite supports. They reported that NH_4-ZSM5 and NH_4-Y zeolites have benefits of Mn–Ni such as decreasing the coke formation, decreasing the Ni particle size, and increasing the Ni dispersibility, although the addition of Mn generally engenders decreasing activity.

Fe–Ni. Many studies have investigated effects of Fe–Ni on DRM. Tomishige *et al.*[99] published a minireview on Ni–Fe alloy catalysts for reforming hydrocarbon including DRM in

Table 4 The effect of Ni-based alloy catalysts for DRM

	Properties of metal		Catalytic performance			Resistance			
	Metal reductivity	Metal dispersion	Activity	Selectivity	Long-term stability	Coke	Sulphur	Sintering	Remarks
Mn–Ni		High	Low/high		High	High			Mn could increase the coke resistance
Fe–Ni			High		High	High			The oxidation and reduction of Fe occur during DRM, which results in high coke resistance
Co–Ni		High	High	High H_2/CO	High	High	High	High	O species adsorbed on Co due to the strong affinity to oxygen affinity, promoting the gasification of C species
Cu–Ni	High		High/low		High	High		A slight low	The optimal Cu/Ni ratio exists
Zn–Ni					High	High			The dilution of Ni ensembles by Zn could improve the coke resistance
Mo–Ni			High/ low		High				Mo addition to Ni/Al_2O_3 could lead to a decrease in activity, whereas NiMo nanocatalysts on MgO single crystal support showed excellent performance
In–Ni	High		Low			High			The excess amount of In lowers the activity drastically
Sn–Ni			Low			High			Sn atoms occupy the C nucleation site, but the excess amount of Sn lowers the activity drastically
Ru–Ni	High		High/low	Low H_2/CO	High	High			Ru atoms occupy the more active sites, resulting in the lower activity and high coke resistance
Rh–Ni			High						Rh–Ni catalyst shows enhanced methane cracking and coke gasification
Pt–Ni			Low		High	High			Pt reduces the activity of CH_4 decomposition

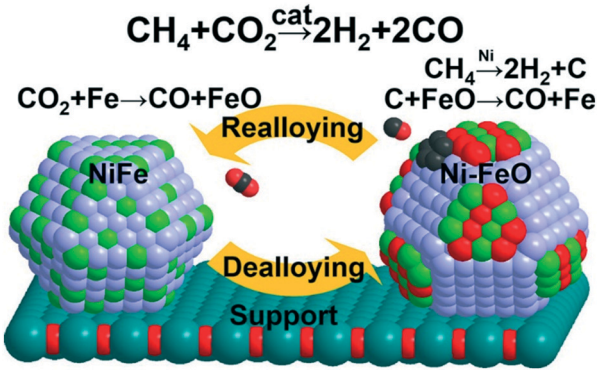

Fig. 12 The schematic image of reaction mechanism of Ni–Fe alloy. Reprinted with permission from ref. 102. Copyright 2017 American Chemical Society. https://pubs.acs.org/doi/abs/10.1021/jacs.6b11487.

2017. In recent years, Song *et al.*[100] investigated a Fe–Ni catalyst supported on Al_2O_3. Also, Margossian *et al.*,[101] Kim *et al.*[102] and Theofanidis *et al.*[103] investigated Ni–Fe catalysts on Mg(Al)O. Gunduz-Meric *et al.*[104] investigated the core–shell NiFe@SiO_2 catalysts. In addition, Theofanidis *et al.*[105] reported improved stability and activity by addition of Pd to Ni–Fe/$MgAl_2O_4$. Furthermore, DFT calculation on the Ni_2Fe overlayer of Ni(111) surface was conducted by Xu *et al.*[106] and by Ray *et al.*[107]

Generally, the reaction mechanism on Ni–Fe catalysts has been demonstrated as presented below.[100]

$$Fe^0 + xCO_2 \rightarrow xCO + FeO_x \quad (9)$$

$$CH_4 \rightarrow 2H_2 + C_\alpha \quad (10)$$

$$FeO_x + C_\alpha \rightarrow Fe^0 + CO \quad (11)$$

Fe^0 metal is oxidized to FeO_x by CO_2. Then carbon species C_α is formed by CH_4 decomposition. Finally, FeO_x and C_α react to form Fe^0 and CO. Furthermore, Kim *et al.*[102] reported structural change during this oxidation–reduction mechanism (Fig. 12). Fe is partially oxidized to FeO and partially de-alloyed to form Ni-rich NiFe alloy; Fe migrates and preferentially forms FeO on the surface. The FeO reacts with C_α and produces CO. The reduced Fe restores the original Ni–Fe alloy. This dynamic mechanism occurring during the DRM reaction provides superior resistance for coke formation.

Song *et al.*[100] reported higher activity and improved coke resistance on Ni–Fe catalysts. Fig. 13 presents the result of activity tests and O_2-TPO of 15.7wt%Ni/Al_2O_3 and 9.5wt%Ni–4.2wt%Fe/Al_2O_3 catalyst after their low-temperature stability tests (723 K, 20 h). The peaks attributed to C_α, C_β and C_γ are assigned according to the oxidation temperature. The formation of C_γ (inactive graphic carbon) was suppressed on the Fe–Ni catalyst. Furthermore, TEM measurements of spent catalysts confirmed that filamentous carbon was not formed on Fe–Ni/Al_2O_3, although it was formed on Ni/Al_2O_3.

Margossian *et al.*[101] investigated the effect of Ni–Fe ratios and reduction temperature of NiFe nanoparticles (3–4 nm) supported by Mg(Al)O prepared by the colloid synthesis. They concluded that NiFe catalysts with a Ni/Fe ratio of 3 reduced at 923 K showed higher stability and activity than Ni catalysts.

In addition, oxide supports containing Fe have been investigated, such as Ni–Fe–Al mixed oxides,[108] $Fe_xNi_yMg_{1-x-y}O$,[109] Ni/$MgFe_xAl_{2-x}O_4$,[110,111] $La_{0.9}Sr_{0.1}Ni_{1-x}Fe_xO_3$,[112] $La_{0.6}Sr_{0.2}Ti_{0.85}Ni_{0.15}O_{3-\delta}$[113,114] and $La_xFe_{1-x}Ni_{0.1}O_{3-\delta}$.[115] For these catalysts, the formation of Ni–Fe alloys was confirmed by the precipitation of metallic particles because of hydrogen reduction. Higher resistance against carbon deposition was reported.

Co–Ni. Many papers describing the effects of Co–Ni alloys on DRM have been published during the last five years (Table 5). The Co–Ni alloy catalysts show high activity not only at high temperatures but also at low temperatures,[116] high durability to carbon, and improved S tolerance.[117] Many reports have described the existence of an optimal Co/Ni ratio, but the value varies depending on the catalyst. In addition, *in situ* XPS,[116] and *in situ* scanning transmission X-ray microscopy (STXM)[118,119] studies have been conducted recently.

In general, Co has a strong affinity to oxygen; O species preferentially adsorb on Co, which has the effect of promoting the gasification of C species.[120–123] Sheng *et al.*[124]

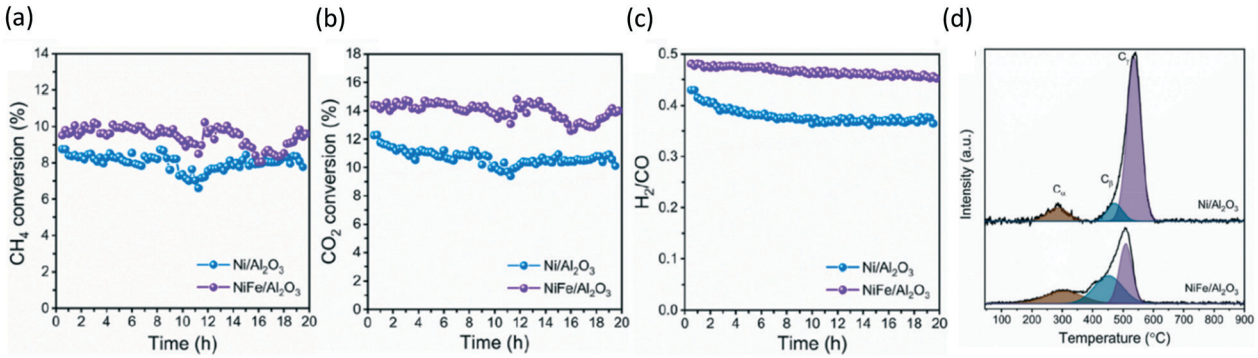

Fig. 13 The results of long-term stability tests over 15.7wt%Ni/Al_2O_3 and 9.5wt%Ni–4.2wt%Fe/Al_2O_3 at low temperature (450 °C, 20 h). (a) CH_4 conversion (b) CO_2 conversion (c) H_2/CO ratio, and (d) O_2-TPO spectra of spent catalysts. Reprinted with permission from ref. 100. Copyright 2020 American Chemical Society. https://pubs.acs.org/doi/10.1021/acs.iecr.0c01204.

Table 5 Summary of Co–Ni catalysts reported in recent years

Catalysts	Preparation	Reaction condition	Activity	Sel.	Stability	Remarks	Ref.
10wt%Co–5wt%Ni/γ-Al_2O_3	Co-impregnation	650–700 °C, CH_4 : CO_2 = 1 : 1, 36 L h^{-1} g_{cat}^{-1}	X_{CH_4}, X_{CO_2} = 67–71%, 700 °C	H_2 yield >50%	Stable for 4 h	E_a = 36–40 kJ mol^{-1}, the amorphous carbon was dominant on spent catalyst	126
5wt%Ni–5wt%Co/γ-Al_2O_3	Step-wise impregnation	350–700 °C, CH_4 : CO_2 : N_2 = 1 : 1 : 8, 300 000 mL h^{-1} g_{cat}^{-1}	X_{CH_4} = 76.0% at 700 °C	H_2/CO = 0.93	Stable for 60 h	Active at low temp. It prevents side reactions	117
12wt%NiO–3wt%Co_3O_4/γ-Al_2O_3	Thermo gravimetric method	500–700 °C, CH_4 : CO_2 = 1 : 1, 12 000 mL h^{-1} g_{cat}^{-1}	X_{CH_4} = 53% X_{CO_2} = 58%		Stable for 5 h with carbon deposition	TGPR has advantages of the reduction of the number of synthesis stages	127
6wt%Ni@meshed–*x*wt%Co/γ-Al_2O_3	Wet-impregnation,	450–650 °C, CH_4 : CO_2 = 1 : 1	X_{CH_4} = 70% 75% at 650 °C		Stable for 70 h with a little decrease of activity	Mesh-like Co coating structure showed high activity and coking resistance	128
$NiCoO_x$/γ-Al_2O_3 (no data for Ni loading)	Reverse micellar method	800 °C, CH_4 : CO_2 : N_2 = 7 : 9.5 : 83.5	X_{CH_4} = 86% X_{CO_2} = 77%		Stable for 2 h	*In situ* STXM were conducted	119, 120
5wt%Ni–5wt%Co/FSP-Al_2O_3	Co-impregnation	500–800 °C, CH_4 : CO_2 : N_2 = 1 : 1 : 1, 144 L h^{-1} g_{cat}^{-1}				Co; a high affinity for the removal of carbon species by oxidation, Ni; highly active for CH_4 decomposition	129
5wt%Ni–5wt%Co/θ-Al_2O_3		700 °C, CH_4 : CO_2 : Ar = 1 : 1 : 1, 6000 h^{-1}	X_{CH_4} = 75% X_{CO_2} = 82%	H_2/co = 1.3	Deactivation occurred	The rapid decrease of activity due to phase transition	130
2.5wt%Ni–2.5wt%Co/Al_2O_3–ZrO_2		700 °C, CH_4 : CO_2 : N_2 = 17 : 17 : 11, 18 000 mL h^{-1} g_{cat}^{-1}	X_{CH_4} = 91%	H_2/CO = 0.96	Stable for 28 h	High metal dispersion of Ni–Co cat The catalyst was calcined at 973 K	131
2.5wt%Ni–2.5wt%Co/mesoporous SiO_2	Deposition–precipitation technique	700 °C, CH_4 : CO_2 : He = 1 : 1 : 8, 50 000 mL h^{-1} g_{cat}^{-1}	X_{CH_4}, X_{CO_2} ≈ 90%	H_2/CO ≈ 1	Stable for 200 h	The coexistence of nano-sized Co and Ni in the mesopore resulted in better stability	124
Ni–Co/SiO_2 with various Ni/Co ratios, total 10 wt%	Hydrothermal method with urea	750 °C, CH_4 : CO_2 : He = 1 : 1 : 1, 60 000 mL h^{-1} g_{cat}^{-1}	X_{CH_4} ≈ 84% X_{CO_2} ≈ 86% at 1023 K	H_2/CO ≈ 0.8	Stable for 100 h	Co could enhance the metal–support interaction catalysts with Ni/Co = 7/3 showed high and stable activity, but others did not	132
Co–Ni/SiO_2, total 10 wt%		750 °C, CH_4 : CO_2 : N_2 = 1 : 1 : 1, 36 000 mL h^{-1} g_{cat}^{-1}	X_{CH_4} = 87% X_{CO_2} = 94% at 1023 K	H_2/CO = 0.84	Stable for 12 h	Catalysts with Ni/Co = 4/1 showed the highest activity	133
Ni–Co/SBA-15 with various Ni/Co ratios, total 10 wt%	Urea co-precipitation	800 °C, CH_4 : CO_2 = 1 : 1, 72 000 mL h^{-1} g_{cat}^{-1}	X_{CH_4} ≈ 86–87% X_{CO_2} ≈ 93–94%	H_2/CO ≈ 1	Stable for 50 h	9wt%Ni–1wt%Co was the best Catalysts with Ni/Co >1 showed improved activity and stability due to the high dispersion of metals, the synergetic effect of Ni and Co, the confinement effect of SBA-15 mesoporous channels	134
(*x*NiyCo)/SBA-15 total 5 wt%	Modified co-impregnation	700 °C, CH_4 : CO_2 = 1 : 1, 30 000–240 000 mL h^{-1} g_{cat}^{-1}	X_{CH_4} ≈ 40% X_{CO_2} ≈ 65%	H_2/CO ≈ 0.6	Stable for 100 h with a slow deactivation	4.5wt%Ni–0.5wt%Co was the best composition, which showed high stability for 100 h	135
Co–Ni/CeO_2 with various Ni/Co ratios, total 10 wt%	Incipient wetness co-impregnation	800 °C, CH_4 : CO_2 : N_2 = 3 : 3 : 4, 12 000 mL h^{-1} g_{cat}^{-1}	X_{CH_4} = 80% X_{CO_2} = 85%	H_2/CO > 0.6	Stable for 10 h	The catalysts with Co/Ni = 0.8 (atomic ratio) showed the highest activity and stability	136

Table 5 *(continued)*

Catalysts	Preparation	Reaction condition	Activity	Sel.	Stability	Remarks	Ref.
1.8wt%Co–1.2wt%Ni/$Ce_{0.75}Zr_{0.25}O_2$						Deactivation due to coke deposition was faster on Ni–Co catalyst supported on $Ce_{0.75}Zr_{0.25}O_2$ than that on a mixture of CeO_2 and ZrO_2	137
1.8wt%Co–1.2wt%Ni/$Ce_{0.8}Zr_{0.2}O_2$/β-SiC	Deposition precipitation with urea	750 °C, CH_4 : CO_2 = 1 : 1, 12 L h^{-1} g_{cat}^{-1}	X_{CH_4} ≈ 65–70% X_{CO_2} ≈ 70–75%	H_2/CO = 0.82	Stable for 550 h	By anchoring of Co–Ni/CZO on β-SiC, sintering, and oxidation of metals could be suppressed, resulting in high stability	138
Ni–Co/Ce–Zr, Ce–La (9.2 atomic % of Ni)	Deposition precipitation with urea	775 °C, CH_4 : CO_2 = 1 : 1, 20–30 ppm sulfur			Stable for sulfur	The addition of Co could improve the sulfur tolerance	118
Co–Ni/H-ZrO_2 with various Ni/Co ratios, total 5 wt%	Co-impregnation	700 °C, CH_4 : CO_2 : Ar = 1 : 1 : 9, 256 L h^{-1} g_{cat}^{-1}	X_{CH_4} = 92.8% X_{CO_2} = 93%	H_2/CO = 0.8	Stable for 6 h with a little decrease of activity	H-ZrO_2 is a mesoporous ZrO_2 hollow sphere 0.89wt%Co–3.83wt%Ni/H-ZrO_2 was the best Carbon deposition on Ni can be oxidized by oxygen on Co	125
4wt%Ni–1wt%Co/CF-La_2O_3 with various Ni/Co ratios	Ultrasonic-assisted impregnation	740 °C, CH_4 : CO_2 : N_2 = 1 : 1 : 1, 14 000 mL h^{-1} g_{cat}^{-1}	X_{CH_4} = 88% X_{CO_2} = 83%	H_2/CO = 1.1	Stable for 10 h	CF (carbon nanofiber) has a high surface area (1393 m^2 g^{-1}) Resistance to Ni-sintering	139
12.5wt%Ni–2wt%Co/CeO_2–$ZnAl_2O_4$	Co-precipitation	700 °C, CH_4 : CO_2 = 1 : 1, 18 000 mL h^{-1} g_{cat}^{-1}	X_{CH_4} = 76%	H_2/CO = 0.99	Stable for 8 h with coke deposition	Increasing surface area, smaller metal particles, stronger active phase/support interaction, higher coke resistance were observed by Co addition	122
2.8wt%Ni–2.8wt%Co/HAP (HAP; $Ga_{10}(PO_4)_6(OH)_2$)	Successive incipient wetness impregnation	700–750 °C, CH_4 : CO_2 : N_2 = 1 : 1 : 3	X_{CH_4} = 73% X_{CO_2} = 79% at 750 °C	H_2/CO = 0.9	Stable for 160 h with an initial decrease of activity	Carbon nanotubes were observed on spent catalysts	140
Ni–Co catalyst from $La(Co_xNi_{1-x})_{0.5}Fe_{0.5}O_3$, total 5 wt%	Sol–gel self-combustion	750 °C, CH_4 : CO_2 = 1 : 1, 12 000 mL h^{-1} g_{cat}^{-1}	X_{CH_4} = 70% X_{CO_2} = 80% at 750 °C		Stable for 30 h	Reduced perovskite catalysts with x = 0.10 or 0.30 showed structural stability, the highest activity, and the most stability for coke deposition	123

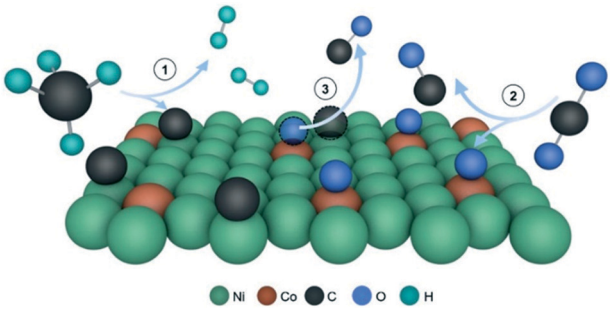

Fig. 14 Schematic image of reaction mechanism on Ni–Co alloy. Reprinted with permission from ref. 124. Copyright 2019 American Chemical Society. https://pubs.acs.org/doi/10.1021/acsami.9b05822.

elucidated the mechanism of CO formation by the reaction of the generated carbon with active oxygen using XPS, XRD, CO_2-TPD, FTIR, *etc.* (Fig. 14).

In addition to high resistance toward carbon deposition, the durability to sulphur has been reported by Jiang *et al.*[117] As shown in Fig. 15, 0.24wt%Ni–0.24wt%Co catalysts supported on ZrO_2–CeO_2 showed drastically improved tolerance for sulphur. They suggested that the Ni–Co interaction is important for the development of sulphur tolerance and discussed the possibility that modification of the electronic state of Ni by Co in the small metal cluster inhibits the adsorption of H_2S.

Wu *et al.*[116] reported high activity, stability, and selectivity at high and low temperatures of 5 wt%Ni–5wt%Co supported on γ-Al_2O_3 catalysts prepared by stepwise impregnation method. The Ni–Co/γ-Al_2O_3 catalyst showed high activity and high H_2/CO ratio, even at temperatures as low as 623 K. The catalyst maintained near-equilibrium conversion and high H_2/CO ratio at 1073 K for 60 h. Strong metal–support interaction contributed to the suppression of sintering. The small metal particle size contributed to the suppression of carbon deposition. *In situ* XPS analysis of the Ni–Co catalyst in a reaction atmosphere at different temperatures showed that the metal was reduced as the reaction temperature

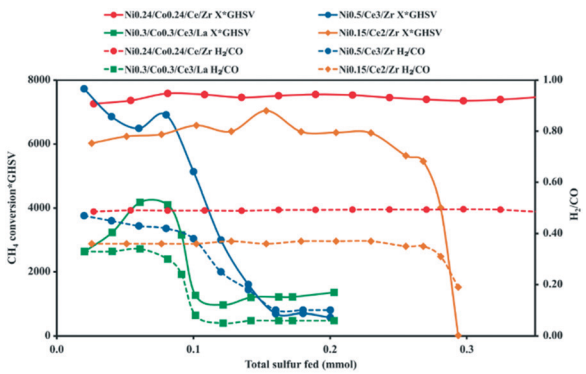

Fig. 15 Activity of Ni–Co catalysts at 1048 K with sulphur feed. Co could improve the sulphur resistance. Reprinted with permission from ref. 117. Copyright 2021 Elsevier.

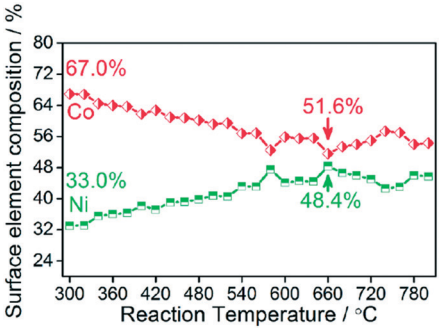

Fig. 16 The changes of surface Ni and co compositions of Ni–Co/Al_2O_3 with increasing temperature was changed, which was determined by *in situ* XPS. Reprinted with permission from ref. 116. Copyright 2019 American Chemical Society. https://pubs.acs.org/doi/10.1021/acscatal.8b02821.

increased, the cobalt content on the surface decreased, and the nickel content increased (Fig. 16).

Results of EXAFS analysis revealed the presence of lattice strain in the Ni–Co alloy, confirming strong interaction between Ni and Co atoms. The lattice-strained Ni–Co has a strong CO_2 dissociation ability, which is responsible for the excellent activity of the DRM reaction, especially in the low-temperature region. In addition, H_2-TPD experiments revealed that hydrogen desorption is enhanced greatly on Ni–Co catalysts, which is a factor suppressing the RWGS reaction.

Askari *et al.*[118,119] investigated Ni–Co alloy catalysts using the technique of *in situ* STXM and showed a different result of *in situ* XPS study by Wu *et al.*[116] Askari *et al.*[118] first prepared $NiCoO_x$/γ-Al_2O_3 catalyst by the modified reverse micellar method, of which compositions are determined by EDX as 56.4 atom% of O, 1.1 atom% of Co, 9.2 atom% of Ni, and 33.3 atom% of Al. Later, STXM studies of $NiCoO_x$/γ-Al_2O_3 catalyst were conducted under Ar, 5%H_2/Ar, and DRM atmosphere. These results are presented in Fig. 17 and 18. The fresh sample shows inhomogeneous distribution of Ni and Co, forming NiO and Co_3O_4 (Fig. 17(a)). Reduction of the catalysts under a 5 wt%H_2/Ar atmosphere at increased temperature revealed that full reduction of the metal finished at 773 K. Furthermore, at 773 K, voids were observed as shown in Fig. 17(b), resulting from reconstruction because of oxygen removal from the lattice. At 973 K, although the metallic states were unchanged, the structure changed drastically. The core–shell structure was formed. The shell was made entirely of Ni. The core is made of Ni and Co Fig. 17(c). Then, STXM under DRM was conducted. Results obtained 1 min later and 120 min later are presented in Fig. 18. These elemental composition maps and the L3-edge spectra showed that the metallic states and the core–shell structure remained during the 120 min DRM reaction. However, the Ni concentration increment was observed at specific locations on the surface, as indicated by the red arrows. In addition, after 120 min under DRM conditions, the formation of Ni-rich branches on the particle surface was

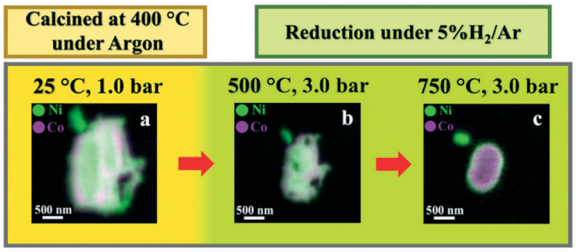

Fig. 17 Elemental mapping of Ni–Co catalysts for (a) fresh calcinated catalyst, (b) catalyst during a reduction under 5%H_2/Ar at 773 K, and (c) catalyst during a reduction under 5%H_2/Ar at 973 K. reprinted with permission from ref. 118. Copyright 2020 American Chemical Society. https://pubs.acs.org/doi/10.1021/acscatal.9b05517.

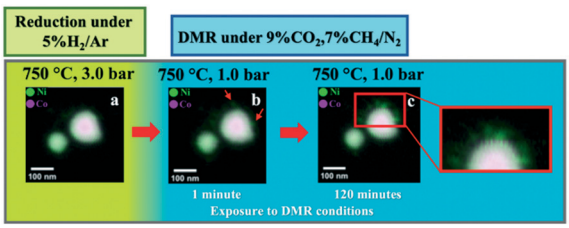

Fig. 18 Elemental mapping of Ni–Co catalysts for (a) catalyst after H_2 reduction, (b) catalyst after 1 min of DRM reaction, (c) catalyst after 120 min of DRM reaction. Reprinted with permission from ref 118. Copyright 2020 American Chemical Society. https://pubs.acs.org/doi/10.1021/acscatal.9b05517.

observed, which might be a result of filamentous carbon on the surface.

Sn–Ni. Guharoy *et al.*[140] and da Silva *et al.*[141] investigated the effects of Sn addition to Ni catalysts. Both concluded that the optimal amount of Sn can suppress coke formation but that excess Sn lowered the activity considerably because Sn atoms occupy the C nucleation sites on Ni and increase the energy barrier for coke nucleation.[140] In addition, DFT calculations and catalytic tests have indicated that Sn promotes the oxidation of key reaction intermediates.[140]

Cu–Ni. Investigations have also elucidated some aspects of Cu–Ni catalysts supported on different oxides supports. Song *et al.*[142] investigated Ni–Cu/Mg(Al)O catalyst. Chatla *et al.*[143] used experimentation and DFT calculation to assess Ni–Cu/Al_2O_3 catalyst. Rezaei *et al.*[144] investigated Ni–Cu/Al_2O_3 catalysts using a microchannel reactor. In addition, Han *et al.*[145] investigated the effects of Ni/Cu ratios in Ni–Cu nanoparticles on SiO_2 supports.

Song *et al.*[142] reported that the amounts of coke formation varied depending on the Cu/Ni ratios. An optimal value exists. The Cu–Ni/Mg(Al)O catalyst with the ratio of Cu/Ni = 0.25–0.5 showed high activity and high stability, whereas the catalysts with higher or lower Cu/Ni ratios deactivated rapidly because of coke formation. Results suggest that the decrease in CH_4 decomposition and increase in CO_2 dissociation attributable to Ni–Cu alloying contributed to suppression of coke deposition for the optimized Ni–Cu catalyst. However, Chatla *et al.*[143] reported Ni–Cu/Al_2O_3 with the ratio Cu/Ni = 1/8 as the best. They concluded that formation of Ni–Cu alloys enhanced the reducibility of NiO and that it enhanced suppression of coke formation. Furthermore, DFT calculation revealed that the higher energy barrier for carbon adsorption makes it easier to remove of the deposited carbon species.

Han *et al.*[145] prepared the Ni–Cu nanoparticles (approximately 5 nm) supported on SiO_2 supports by electrostatic adsorption and investigated the effects of Cu/Ni ratios on activities and stabilities. They described that Ni–Cu/SiO_2 catalyst showed higher activity and less coke formation than Ni/SiO_2, but a little sintering was observed. The catalytic performance varied depending on the Cu/Ni ratios, as shown in Fig. 19. Results showed that the catalyst with the ratio of Cu/Ni = 1/8 exhibited the best performance. Additionally, they suggested the reaction mechanism on Ni–Cu catalysts based on their research and others (Fig. 19), *i.e.*, first, CH_4 molecules are activated on the Ni surface and CH_x and H are formed, second, CO_2 molecules are activated on Cu and CO and O are formed. Finally, CH_x species from CH_4 and O species from CO_2 react on the interface between Ni and Cu, making CO and H_2.

In addition, Wang *et al.*[146] reported effects of Cu-substitution on carbon resistance using $La_2(Ni_{1-x}Cu_x)O_4$ perovskite prepared using a sol–gel method. The $La_2Ni_{0.8}Cu_{0.2}O_4$ after H_2 treatment showed a negligible amount of carbon deposition. The CH_4 conversion and CO_2 conversion were, respectively, 73% and 80%. They concluded that the smaller metal particles of reduced perovskite and the divided Ni ensembles by Cu contributed to the suppression of coke formation.

Zn–Ni. Two groups[147,148] investigated the effect of Zn for ZnO–Al_2O_3 composites supports. Sokolov *et al.*[147] found that Zn-rich supports showed higher activity than Al-rich supports, which they attributed to formation of NiZn alloy or $Ni_3ZnC_{0.7}$. Nataj *et al.*[148] found that although the addition of Zn decreased the surface area, ZnO interfered with formation of the $NiAl_2O_4$ spinel phase, thereby maintaining Ni reducibility. They concluded that catalysts with low Zn/Al ratios were less active and that they were deactivated because of large amounts of carbon deposition, whereas supports with Zn/Al = 1 and 2 remained highly active for a long time.

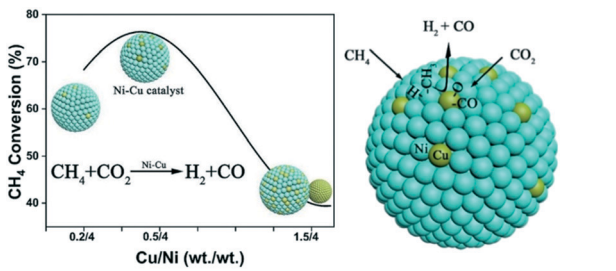

Fig. 19 (Left) The effect of Cu/Ni ratios on CH_4 conversion. (Right) The suggested reaction mechanism on N–Cu catalysts. Reprinted with permission from ref. 145. Copyright 2021 American Chemical Society. https://pubs.acs.org/doi/10.1021/acsanm.1c00673.

That result was attributed to dilution of the Ni ensemble by Ni–Zn alloy formation.

Mo–Ni. Yao *et al.*[149] investigated the effects of Mo addition to Ni/Al_2O_3 catalyst. They concluded that an addition of Mo engenders lowering of the activity because of the weak interaction between NiO species and Al_2O_3, the formation of $MoNi_4$ phase by reduction of $NiMoO_4$ species, and the low basicity of Mo-doped catalysts. In addition, Yao *et al.*[150] prepared a yolk–shell structure (*x*Ni@*y*Mo-HSS, HSS; hollow silica structure). The Mo atoms form a $SiMoO_x$ shell rather than NiMo alloy. Also, $SiMoO_x$ species enhanced the electron cloud density of Ni and the acidity of the support, resulting in increased CH_4 activation. However, the activity of NiMo@HSS was low because of the decrease in the electron cloud density of metal and increased metal particle sizes of NiMo alloy particle.

Song *et al.*[151] prepared Ni–Mo nanocatalysts on single-crystalline MgO (NiMoCat) and reported that the catalyst maintained high activity over 850 h. They first prepared a highly crystalline MgO solid: 3.76wt%Ni and 1.76wt%Mo were loaded to MgO using a polyol-mediated reductive growth method in the presence of a size-limiting polyvinylpyrrolidone (PVP) polymer surfactant. Although Mo itself was not active against DRM, it can enhance the catalytic activity.

The NiMo catalyst maintained high activity during activity tests of over 850 h. No carbon deposition was observed. Moreover, the H_2/CO ratio was almost 1. On the fresh catalyst, the average size of the supported metal was 2.88 nm, but it grew to 17.30 nm within 1 h at 1073 K with flowing of reaction gas. Even after the long-term activity test, the particle size remained the same value at around 17 nm.

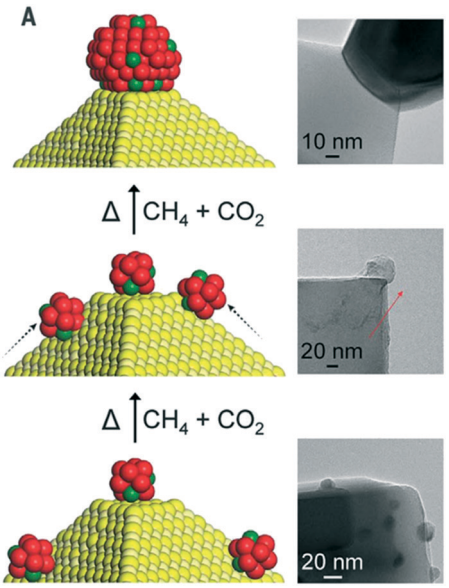

Fig. 20 The schematic image of NanoCatalysts on single crystal edges (NOSCE) technique on NiMoCat. Reprinted with permission from ref. 151. Copyright 2020 AAAS.

Fig. 20 presents TEM images and illustrations of Ni–Mo particles of fresh and spent catalysts. Song *et al.*[151] concluded that the fine particles migrate to the high-energy step edges of crystalline MgO(111) during the reaction, forming stable and persistent particles with average size of 17 nm. Covering the high-energy step edges can be expected to prevent further sintering while eliminating risks of MgO participation in the catalytic reaction.

In–Ni. Liu *et al.*[152] prepared and investigated the Ni-In intermetallic alloy covered by SiO_2. Even the sample with only 0.1wt%In showed excellent coking resistance in the DRM reaction. Results obtained from H_2-TPR revealed that the addition of In led to decreased reduction temperature. The optimum In loading amount was 0.5 wt% considering the balance between carbon-resistance and DRM reactivity; low In loading tended to decrease the coking resistance, whereas high In loading decreased the catalytic activity because of the formation of $InNi_3C_{0.5}$ species. The increased electron density of Ni by electron transfer from In might weaken the ability of Ni to activate C–H bonds and reduce the CH_x cracking process, resulting in the suppression of carbon deposition.

Károlyi *et al.*[153] similarly investigated a 2wt%In–3wt%Ni catalyst supported on SiO_2. They found that diluting the Ni surface can suppress carbon deposition.

5.2 Addition of noble metals to Ni catalysts

This chapter summarizes the effects of adding a small amount of noble metals (Ru, Rh, Re, Pt) to supported Ni catalysts on DRM.

Ru–Ni. Small loadings (<1 wt%) of Ru on Ni catalysts on various supports have been investigated. Álvarez *et al.*[154] investigated the 0.5wt%Ru–15wtNi catalyst supported on MgO/Al_2O_3. Luisetto *et al.*[155] investigated 0.5wt%Ru–10wt%Ni catalyst supported on γ-Al_2O_3. Also, Wysocka *et al.*[156] investigated 1wt%Ru-7wt%Ni on various supports (SiO_2, Al_2O_3, $MgAl_2O_4$, ZrO_2). Álvarez *et al.*[154] and Luisetto *et al.*[155] found that the Ru can improve long-term stability by suppressing coke formation. Luisetto *et al.*[155] explained that the property of Ru which favours carbon gasification contributes to inhibition of coke formation. Álvarez *et al.*[154] claimed that Ru atoms were located on the surface of more active sites, such as step or edge sites because of the low solubility between Ni and Ru. They described that this effect of Ru might be the reason for the lessened activity of Ru-doped catalysts. Luisetto *et al.*[155] stated that Ru can improve not only stability, but also the activity, by keeping the Ni metal reduced. Wysocka *et al.*[156] reported that the activity order as $Ru–Ni/Al_2O_3 > Ru–Ni/MgAl_2O_4 > Ru–Ni/ZrO_2 > Ru–Ni/SiO_2$. This order is the same as that of Ni-loaded catalysts. Also, $Ru–Ni/Al_2O_3$ showed long-term stability for 6 h. They also described that introduction of Ru enhanced methane dissociation, causing the low H_2/CO ratio.

As described in chapter 3 and in 4.2, the Ru–Ni section of chapter 4, Yoon *et al.*[60] investigated carbon deposition using DFT on Ni and Ni–Ru alloys. They claimed that, to predict

the catalytic efficiency and carbon deposition properly, one must investigate not only the dissociation into CH_3, CH_2, CH, C, and H, but also the CO gas evolution reaction (details were presented in chapter 3). The theoretical calculation showed that Ni–Ru catalysts had more stability than either Ni or Ni–Rh.

In addition, Zhou *et al.*[157] prepared $Ru_xNi_yMg_{1-x-y}O$ catalysts using the solvothermal synthesis. The catalysts obtained using the direct reduction method were highly active and stable. Actually, Ru was found to change the type of carbon deposition from a persistent graphitic one that can only be removed by O_2 to a soft system that can be readily removed by CO_2. Furthermore, Ru increased the activation barrier of CH_4 dissociation, thereby slowing the carbon deposition rate.

Rh–Ni. Mozammel *et al.*[158] prepared RhNi, NiCo, and NiCoRh catalysts supported on mesoporous alumina (MAl). These alloy catalysts showed better stability and conversion than the respective mono-metal catalysts. Among these catalysts, 4.5wt%Rh–4.5wt%Ni/MAl showed the highest activity and stability because of the enhanced methane cracking and carbon gasification on alloy surface. They also found that nickel formed a homogeneous alloy phase with cobalt, but a heterogeneous bimetallic phase with rhodium. Alloying with cobalt moderated coking but alloying with rhodium promoted carbon gasification through hydrogen spillover effects. Furthermore, Rh-supported catalysts were less active than Rh-alloyed catalysts, indicating that Rh alloying increased the activity of monometallic catalysts by alloying.

Romano *et al.*[159] reported that the addition of noble metals to Ni catalysts increased the reducibility of the metal, but it had no significant effect on TOF or stability. They prepared Ni, Rh, and Pd supported catalysts and Ni-based alloy catalysts with a few noble metals by the incipient wetness impregnation. They conducted screening tests. Fig. 21 shows H_2-TPR results for the Ni monometallic catalysts and Ni-based alloy catalysts. In fact, Ni/Al_2O_3 shows a NiO reduction peak with a peak top at 711 K and a Ni–O–Al reduction peak with a peak top at 838 K. However, the reduction temperature of the alloy catalyst with a small amount of noble metal was much lower. Only one peak was observed for the Rh–Ni catalyst. Enhancement of the Ni reducibility by the addition of noble metals is attributable to the higher ability to dissociate hydrogen.

Re–Ni. Zubenko *et al.*[160] prepared perovskite precursors based on lanthanum ferrite ($LaFeO_3$), which were subsequently doped with Ni and Re phases. Fig. 22 shows a schematic image of the possible structure of catalysts by co-exsolution from the ceramic precursor. For this study, Re-alloy nanoparticles (Ni–Fe, Re–Fe, Re–Ni–Fe) were formed from composite precursors under reducing conditions. They were found to be active and stable under dry reforming conditions. The Re nanoparticles were not highly active up to 1173 K, whereas the Ni nanoparticles were more active with the addition of Re, even at low temperatures. It was concluded that, because of the strong catalyst–support interaction, the deposition of carbon, the sintering of nanoparticles, and the evaporation of the Re-containing phase were limited.

Pt–Ni. Egelske *et al.*[161] prepared a series of Ni–Pt catalysts supported on γ-Al_2O_3 with 5.0 wt%Ni and up to 2.8wt%Pt by the electroless deposition. Then they evaluated their catalytic performance for DRM. At temperatures below 873 K, the activity of 0.4 layers of Pt was maximal. In fact, it exceeded that of undeposited Ni. However, at 973 K, all samples were deactivated. At high temperatures (973 K), the alloy phase of the nanoparticles separated, which was consistent with the phase diagram of the bulk. The Pt-rich ensemble promoted the activation of CH_4 to coke causing deactivation.

Vasiliades *et al.*[162] intensively studied details of DRM activity and carbon deposition of Pt–Ni alloy catalysts. DRM was conducted at 1023 K using 5 wt%Ni, 0.5wt%Pt, and their binary alloy (5wt%Ni–0.5wt%Pt) supported on $Ce_{0.8}Pr_{0.2}O_{2-\delta}$ support. The origin of the deposited carbon during the DRM was quantified using isotopically labelled $^{13}CO_2$ as the feed

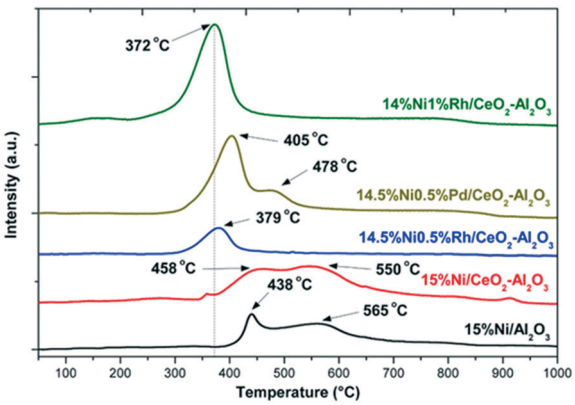

Fig. 21 The H_2-TPR spectra of various Ni monometallic catalysts and Ni-based alloy catalysts. Reprinted with permission from ref. 159. Copyright 2021 Elsevier.

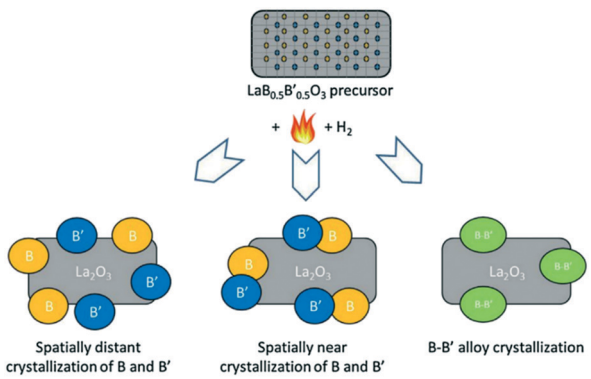

Fig. 22 The schematic image of the possible structure of co-exsolution of B and B′ from an ordered ceramic precursor $LaB_{0.5}B'_{0.5}O_3$ by H_2 reduction. Reprinted with permission from ref. 160. Copyright 2017 Elsevier.

gas. Results showed that the carbon deposition on supported Ni and Ni–Pt alloys was mainly attributable to the CH_4 decomposition on the metal surface, whereas that on supported Pt was attributable to the CO disproportionation reaction. The Ni–Pt catalyst was found to have a significantly lower rate of carbon deposition despite a smaller decrease in the CH_4 conversion rate compared to the monometallic Ni catalyst. The Ni–Pt catalyst showed overall excellent performance and stability after 50 h of use at 1023 K DRM, with a low amount of deposited carbon of 0.38 wt%.

5.3 Others

In recent years, catalysts supported with not only two-metal but also three-metal and Co-based alloy catalysts have been developed.

Trimetallic catalysts

Co–Fe–Ni. Joo *et al.*[52] reported that exsolved Co–Ni–Fe ternary alloy supported on perovskite $PrBaMn_{1.7}Co_{0.1}Ni_{0.2}O_{5+\delta}$ had enhanced activity compared to either Co–Ni or Ni supported catalysts. They calculated the d-band centres of Co–Ni–Fe, Co–Ni, and Ni, and concluded that the upshift of the d-band centre can be attributed to the higher activity of Co–Ni–Fe.

Co–Cu–Ni. Ghanbarabadi and Khoshandam[126] investigated Ni–Co, Ni–Cu, bimetallic nanocatalysts, and Ni–Co–Cu trimetallic nanocatalysts supported on γ-Al_2O_3. Their order of activity was Ni–Co/γ-Al_2O_3, Ni–Co–Cu/γ-Al_2O_3, and Ni–Cu/γ-Al_2O_3. Moreover, results showed that Ni–Co was more active than Ni–Co–Cu. However, the TPO results demonstrated that the amount of coke formation in Ni–Co–Cu was reduced by the presence of Cu.

Co–Mn–Ni. Kim *et al.*[163] investigated the tri-metallic, reduced $LaNi_{0.34}Co_{0.33}Mn_{0.33}O_3$ perovskite catalysts. The catalyst showed higher activity and stability with less coke formation than either $LaNi_{0.5}Co_{0.5}$ or $LaNiO_3$. Results showed that Mn can enhance the stability and that Co can enhance the activity.

Co–Ru–Ni. Aramouni *et al.*[164] investigated Co–Ni–Ru trimetallic catalysts supported on Al(Mg)O with various Co/Ni ratios and calcination temperatures. The high Ni/Co ratio was good for activity and stability. The high oxygen affinity of Co was effective for inhibiting carbon deposition. The addition of Ru also improved the stability and coke resistance of the tested Ni–Co catalysts, although the activity at high-temperature calcination was reduced slightly.

Fe–Cu–Ni. Jin *et al.*[165] investigated the trimetallic NiFeCu catalysts supported on Mg(Al)O with various Cu ratios. Results showed that Cu addition improved the coke resistance of Ni–Fe catalysts, with $Ni_3Fe_1Cu_1$ catalyst being the most durable.

Fe–Pd–Ni. Theofanidis *et al.*[105] reported enhanced activity and stability of the Pd-added Ni–Fe/$MgAl_2O_4$ catalyst. Core–shell structures, of which the core is Fe–Ni and the shell is Fe–Ni–Pd, were observed after the reduction. Because of the structure, the segregation of Fe on the surface can be suppressed.

Co-based catalysts. Supported Co catalysts have also been studied in DRM because of their low cost and large-scale availability.[166] Bradford and Vannice[167] provide a summary of Co catalysts on various supports. Furthermore, San-José-Alonso *et al.*[168] reported higher activity of Co or Co-rich Ni catalysts for DRM because of the high ability of Co for CH_4 decomposition, but much carbon deposition was observed on these catalysts. Consequently, Co catalysts are promising catalysts, but they are necessary for additional development. However, Co catalysts have not been studied as much as Ni and noble metal catalysts have been. This section summarizes information related to Co-based alloy catalysts that have been reported in recent years.

Xie *et al.*[169] reported synergetic effects of Co and Pt on DRM activity and H_2/CO selectivity. Using the co-impregnation method, Co–Pt alloy, of which the Pt/Co molar ratio is 1/3, supported on CeO_2 was prepared. During the reaction, the Pt and Co maintained their metallic state, but there was slight oxygen decoration, resulting in oxygen–metal site pairs (O*–*). Kinetic studies and DFT calculation revealed that the catalytic surface of PtCo/CeO_2 with O*-modified formation promotes the activation of C–H bonds. In addition, PtCo/CeO_2 catalysts were resistant to coke formation compared to Pt/CeO_2. They can be regenerated easily by a mild CO_2 treatment. In addition, Itkulova *et al.*[166] investigated Co catalysts with a small amount of Pt supported on Al_2O_3–ZrO_2 for DRM and bi-reforming. Results indicate that 5 wt%Co–Pt(95 : 5)/Al_2O_3–ZrO_2 showed high stability and no sintering or coke formation observed during the 100 h activity tests.

Perovskite-based catalysts $LaCoO_3$ and $LaCu_{0.55}Co_{0.45}O_3$ were prepared and investigated by Touahra *et al.*[170] The $LaCu_{0.55}Co_{0.45}O_3$ catalyst showed higher catalytic performance and higher carbon resistance in DRM than the $LaCoO_3$ catalyst. The high catalytic performance of the $LaCu_{0.55}Co_{0.45}O_3$ catalyst was attributed to the strong Cu–Co interaction observed after reduction, which suppressed carbon formation and particle aggregation. In addition, the carbon species formed on the Co sites are well removed by the oxygen species generated from $La_2O_2CO_3$.

6. Summary and perspectives

This paper summarizes recent research on alloys in SRM and DRM, mainly emphasizing Ni-based catalysts. The Ni catalyst is promising as an industrial catalyst because of its low cost and high activity, but the deactivation of the catalyst because of carbon deposition is an issue. Although noble metal catalysts are superior to Ni catalysts in terms of their activity and durability, they are difficult to industrialize because of their high costs. Therefore, the mainstream development is designed to improve the catalytic performance of Ni catalysts by adding various secondary metals. Actually, Ni-based alloys of many various types have been reported, including Ni-based alloy catalysts with base metals (Mn, Fe, Co, Cu, Zn, Mo, In, Sn, *etc.*) and Ni-based alloy catalysts with noble

metals (Ru, Rh, Ag, Re, Ir, Pt, Au, *etc.*). Even noble metal doped catalysts are reported to improve performance, in many cases by a small amount of noble metal doping, which does not lead to high cost. Alloying Ni catalysts enables to succeed in developing an ideal catalyst that is both inexpensive and has excellent catalytic performance.

As for catalyst preparation, many catalysts were prepared with metals supported on oxide supports such as Al_2O_3, whereas others were catalysts with Ni or Ni-based alloy nanoparticles deposited on the surface by reduction of oxides (such as perovskite oxides) containing Ni and secondary metals in their composition. The alloy effects were reported to improve the dispersion and reducibility of the supported metal, to change the catalytic performance such as activity and selectivity, and to improve the durability against carbon deposition, sulphur poisoning, and sintering, and so on. Tables 3 (for SRM) and 4 (for DRM) summarize the Ni-based alloy catalyst effects reported herein. However, alloy effects often vary with catalysts, compositions, and reaction conditions. Some papers present different results. Therefore, it is noteworthy that Tables 3 and 4 show only representative features of a few alloy catalysts presented herein.

This section presents a brief summary of the effects of the addition of secondary metals by reviewing Tables 3 and 4.

(1) Properties of metal

Numerous reports have described that the addition of a secondary metal changes the properties, such as reducibility and dispersibility, of the supported metal. The improvement of reducibility is remarkably pronounced for Ni catalysts doped with noble metals, as shown in Fig. 21, where marked reduction of the reduction temperature was observed by adding Rh or Pd to Ni catalysts.[159] The high hydrogen dissociation capacity of the noble metals might be a factor in the high activity of the catalysts. The addition of a second metal was also found to improve the Ni dispersion in several alloys (Mn–Ni,[97,98] Co–Ni,[116] Rh–Ni,[76] Ir–Ni,[83] Pt–Ni,[84] *etc.*). As discussed in chapter 3, the Ni particle size has a significant effect on the ease of carbon deposition. Actually, carbon deposition is less likely to occur on highly dispersed small Ni particles. Therefore, alloying to reduce the Ni particle size is very effective for inhibiting carbon deposition.

(2) Catalytic performance

Whereas the activity of the Ni catalyst decreases during the reaction, most papers surveyed in this report have described the improved stability of many alloy catalysts after long-term stability tests (Tables 3 and 4). However, regarding the activity, some reports (especially for precious metal) have described that the addition of a second metal increased the activity, although others did not. The DFT calculations of some alloy surfaces showed that the CH_4 dissociation barrier increases compared to Ni (Au–Ni,[61] Ir–Ni,[83] Pt–Ni,[42] Ru–Ni,[157] *etc.*). Some experimental reports showed that TOF increases or that activation energy increases (Sn–Ni,[66] Ag–Ni,[80] Pt–Ni,[42] *etc.*). In addition, a decrease in activity because of occupation of more active, or low-coordinated Ni sites by second metals (Au–Ni,[48] Ag–Ni,[82] Ru–Ni,[154] Co–Ni,[65] Sn–Ni,[66,140] *etc.*) was reported. Consequently, probably methane activity tends to decrease with the addition of the second metal. However, some reports have described that the overall activity increased because of the effect of improving the reducibility and dispersibility of the metal by adding a secondary metal (Au–Ni,[86] and other precious metal addition). In addition, the change of selectivity was reported for some alloy catalysts for DRM (Cu–Ni,[72] Rh–Ni,[76] and Re–Ni[81] for SRM; and Co–Ni[116] and Ru–Ni[155]).

(3) Stability

In addition to the ability of alloy catalysts to inhibit carbon deposition, their abilities to inhibit sulphur poisoning and sintering were investigated. First, almost all reports have described that alloying improved the inhibition of carbon deposition and that it showed stable activity in long-term tests (Tables 3 and 4). For example, in the Fe–Ni system,[100] the type of deposited carbon was evaluated by O_2-TPO. Stable and difficult to react species of carbon was decreased by alloying (Fig. 13). Some papers have explained that the reason for the suppression of carbon deposition as the second metal blocks the more active site of Ni, such as edge sites or step sites, thereby preventing carbon nucleation. Other factors such as a decrease in the Ni particle size, dilution of the Ni ensemble, and decrease in stability of the C species on the alloy surface (*e.g.* Au–Ni,[61] Cu–Ni[143]) were also reported. In addition, a mechanism was proposed for Co–Ni in which O is adsorbed preferentially onto Co; it reacts with C species formed on Ni, leading to CO gasification (Fig. 14).[124] However, many reports have described that either too little or too much was not beneficial. For example, Sn–Ni can suppress carbon deposition, but too much Sn–Ni engenders a significant decrease in SRM activity (Fig. 12).[73] Cu–Ni shows high activity and durability at the optimum Cu/Ni ratio, but too much or too little Cu–Ni engenders rapid deactivation of activity because of severe carbon deposition.[143]

Some studies have assessed durability against sulphur, such as Fe–Ni[67] and Au–Ni[88] for SRM, and Co–Ni[118] for DRM (Fig. 15). Furthermore, the sintering was reportedly suppressed for Rh–Ni[77] and Ir–Ni[77] in SRM, and Co–Ni[116] in DRM.

Although it is gratifying to see that almost all the alloy catalysts reportedly have improved durability against carbon deposition, apparently some room remains for additional research and development of catalysts with sulphur resistance, sintering suppression, and high activity at low temperatures. In addition, only a few studies have tested various alloy catalysts under the same conditions. It is still difficult to discuss which alloy catalyst has the best catalytic performance. Future studies should be undertaken to develop catalysts that not only have durability against carbon deposition, but which also have resistance to sulphur and sintering, and high activity even at

low temperatures. To develop such materials, more research must be done to elucidate bi-metallic and tri-metallic catalysts, with consideration of the various properties of the respective metals. For such purpose, high-throughput screening system for multi-metal alloy catalysts and high-performance calculation will be important in future.

Conflicts of interest

There are no conflicts to declare.

Notes and references

1 L. Liu and A. Corma, *Chem. Rev.*, 2018, **118**, 4981–5079.
2 M. Zhou, C. Li and J. Fang, *Chem. Rev.*, 2021, **121**, 736–795.
3 V. Ponec, *Appl. Catal., A*, 2001, **222**, 31–45.
4 R. Ferrando, J. Jellinek and R. L. Johnston, *Chem. Rev.*, 2008, **108**, 845–910.
5 S. Furukawa and T. Komatsu, *ACS Catal.*, 2017, **7**, 735–765.
6 T. Zhang, A. G. Walsh, J. Yu and P. Zhang, *Chem. Soc. Rev.*, 2021, **50**, 569–588.
7 R. T. Hannagan, G. Giannakakis, M. Flytzani-Stephanopoulos and E. C. H. Sykes, *Chem. Rev.*, 2020, **120**, 12044–12088.
8 Y. Xin, S. Li, Y. Qian, W. Zhu, H. Yuan, P. Jiang, R. Guo and L. Wang, *ACS Catal.*, 2020, **10**, 11280–11306.
9 D. Wu, K. Kusada, T. Yamamoto, T. Toriyama, S. Matsumura, S. Kawaguchi, Y. Kubota and H. Kitagawa, *J. Am. Chem. Soc.*, 2020, **142**, 13833–13838.
10 S. Furukawa, T. Komatsu and K. I. Shimizu, *J. Mater. Chem. A*, 2020, **8**, 15620–15645.
11 P. Liu and J. K. Nêrskov, *Phys. Chem. Chem. Phys.*, 2001, **3**, 3814–3818.
12 M. Mohamedali, A. Henni and H. Ibrahim, *ChemEngineering*, 2018, **2**, 1–23.
13 J. N. Armor, *Appl. Catal., A*, 1999, **176**, 159–176.
14 M. A. Peña, J. P. Gómez and J. L. G. Fierro, *Appl. Catal., A*, 1996, **144**, 7–57.
15 A. Iulianelli, S. Liguori, J. Wilcox and A. Basile, *Catal. Rev.: Sci. Eng.*, 2016, **58**, 1–35.
16 Q. Wang, X. Chen, A. N. Jha and H. Rogers, *Renewable Sustainable Energy Rev.*, 2014, **30**, 1–28.
17 J. R. Rostrup-Nielsen, *J. Catal.*, 1984, **85**, 31–43.
18 J. G. Xu and G. F. Froment, *AIChE J.*, 1989, **35**, 88–96.
19 D. Li, Y. Nakagawa and K. Tomishige, *Appl. Catal. A*, 2011, **408**, 1–24.
20 H. Wu, V. La Parola, G. Pantaleo, F. P. Puleo, A. M. Venezia and L. F. Liotta, *Catalysts*, 2013, **3**, 563–583.
21 E. Meloni, M. Martino and V. Palma, *Catalysts*, 2020, **10**, 352.
22 L. Chen, Z. Qi, S. Zhang, J. Su and G. A. Somorjai, *Catalysts*, 2020, **10**, 858.
23 H. Zhang, Z. Sun and Y. H. Hu, *Renewable Sustainable Energy Rev.*, 2021, **149**, 111330.
24 C. Wang, Y. Wang, M. Chen, D. Liang, Z. Yang, W. Cheng, Z. Tang, J. Wang and H. Zhang, *Int. J. Hydrogen Energy*, 2021, **46**, 5852–5874.
25 I. V. Yentekakis, P. Panagiotopoulou and G. Artemakis, *Appl. Catal., B*, 2021, **296**, 120210.
26 Z. Bian, S. Das, M. H. Wai, P. Hongmanorom and S. Kawi, *ChemPhysChem*, 2017, **18**, 3117–3134.
27 M. A. A. Aziz, H. D. Setiabudi, L. P. Teh, M. Asmadi, J. Matmin and S. Wongsakulphasatch, *Chem. Eng. Technol.*, 2020, **43**, 661–671.
28 T. Yabe and Y. Sekine, *Fuel Process. Technol.*, 2018, **181**, 187–198.
29 V. V. Nedolivko, G. O. Zasypalov, A. V. Vutolkina, P. A. Gushchin, V. A. Vinokurov, L. A. Kulikov, S. V. Egazar'yants, E. A. Karakhanov, A. L. Maksimov and A. P. Glotov, *Russ. J. Appl. Chem.*, 2020, **93**, 765–787.
30 M. A. A. Aziz, H. D. Setiabudi, L. P. Teh, N. H. R. Annuar and A. A. Jalil, *J. Taiwan Inst. Chem. Eng.*, 2019, **101**, 139–158.
31 L. P. Teh, H. D. Setiabudi, S. N. Timmiati, M. A. A. Aziz, N. H. R. Annuar and N. N. Ruslan, *Chem. Eng. Sci.*, 2021, **239**, 116606.
32 Z. Li, Q. Lin, M. Li, J. Cao, F. Liu, H. Pan, Z. Wang and S. Kawi, *Renewable Sustainable Energy Rev.*, 2020, **134**, 110312.
33 R. Singh, A. Dhir, S. K. Mohapatra and S. K. Mahla, *Biomass Convers. Biorefin.*, 2020, **10**, 567–587.
34 Z. Qin, J. Chen, X. Xie, X. Luo, T. Su and H. Ji, *Environ. Chem. Lett.*, 2020, **18**, 997–1017.
35 K. Wittich, M. Krämer, N. Bottke and S. A. Schunk, *ChemCatChem*, 2020, **12**, 2130–2147.
36 E. Kikuchi, S. Tanaka, Y. Yamazaki and Y. Morita, *Bull. Jpn. Pet. Inst.*, 1974, **16**, 95–98.
37 J. R. Anderson and M. Boudart, *Catalysis Science and Technology*, 1984, vol. 5.
38 P. Ferreira-Aparicio, A. Guerrero-Ruiz and I. Rodríguez-Ramos, *Appl. Catal., A*, 1998, **170**, 177–187.
39 I. D. Iglesias, G. Baronetti and F. Mariño, *Energy Sources, Part A*, 2017, **39**, 129–133.
40 M. S. Fan, A. Z. Abdullah and S. Bhatia, *ChemCatChem*, 2009, **1**, 192–208.
41 K. H. Delgado, L. Maier, S. Tischer, A. Zellner, H. Stotz and O. Deutschmann, *Catalysts*, 2015, **5**, 871–904.
42 S. Roy, S. Hariharan and A. K. Tiwari, *J. Phys. Chem. C*, 2018, **122**, 10857–10870.
43 P. M. Hundt, M. E. Van Reijzen, H. Ueta and R. D. Beck, *J. Phys. Chem. Lett.*, 2014, **5**, 1963–1967.
44 S. Nave, A. K. Tiwari and B. Jackson, *J. Phys. Chem. A*, 2014, **118**, 9615–9631.
45 F. Abild-Pedersen, J. Greeley and J. K. Nørskov, *Catal. Lett.*, 2005, **105**, 9–13.
46 A. M. Ranjekar and G. D. Yadav, *J. Indian Chem. Soc.*, 2021, **98**, 100002.
47 C. Vogt, J. Kranenborg, M. Monai and B. M. Weckhuysen, *ACS Catal.*, 2020, **10**, 1428–1438.
48 K. de Oliveira Rocha, C. M. P. Marques and J. M. C. Bueno, *Chem. Eng. Sci.*, 2019, **207**, 844–852.
49 A. Nilsson, L. G. M. Pettersson, B. Hammer, T. Bligaard, C. H. Christensen and J. K. Nørskov, *Catal. Lett.*, 2005, **100**, 111–114.

50 B. Hammer and J. K. Nørskov, *Adv. Catal.*, 2000, **45**, 71–129.
51 B. Hammer and J. K. Nørskov, *Surf. Sci.*, 1995, **343**, 211–220.
52 S. Joo, K. Kim, O. Kwon, J. Oh, H. J. Kim, L. Zhang, J. Zhou, J. Q. Wang, H. Y. Jeong, J. W. Han and G. Kim, *Am. Ethnol.*, 2021, **19104**, 15912–15919.
53 K. Ray, R. Bhardwaj, B. Singh and G. Deo, *Phys. Chem. Chem. Phys.*, 2018, **20**, 15939–15950.
54 S. Arora and R. Prasad, *RSC Adv.*, 2016, **6**, 108668–108688.
55 D. L. Trimm, *Catal. Rev.: Sci. Eng.*, 1977, **16**, 155–189.
56 J. R. Rostrup-Nielsen and D. L. Trimm, *J. Catal.*, 1977, **48**, 155–165.
57 D. L. Trimm, *Catal. Today*, 1999, **49**, 3–10.
58 J. Rostrup-Nielsen, *Catal. Today*, 2006, **111**, 4–11.
59 J. R. Rostrup-Nielsen, J. Sehested and J. K. Noerskov, *Adv. Catal.*, 2002, **47**, 65–139.
60 Y. Yoon, H. Kim and J. Lee, *J. Power Sources*, 2017, **359**, 450–457.
61 F. Besenbacher, I. Chorkendorff, B. S. Clausen, B. Hammer, A. M. Molenbroek, J. K. Nørskov and I. Stensgaard, *Science*, 1998, **279**, 1913–1915.
62 Y. Liu, Y. Chen, H. Yu, F. Guan, Z. Hou, D. Cui and Y. Zhang, *Catal. Today*, 2021, **369**, 167–174.
63 C. H. Bartholomew, *Catal. Rev.: Sci. Eng.*, 1982, **24**, 67–112.
64 J. H. Kim, D. J. Suh, T. J. Park and K. L. Kim, *Appl. Catal., A*, 2000, **197**, 191–200.
65 X. You, X. Wang, Y. Ma, J. Liu, W. Liu and X. Xu, *ChemCatChem*, 2014, **6**, 3377–3386.
66 E. Nikolla, J. Schwank and S. Linic, *J. Catal.*, 2009, **263**, 220–227.
67 M. V. Tsodikov, S. S. Kurdymov, G. I. Konstantinov, V. Y. Murzin, O. V. Bukhtenko and Y. V. Maksimov, *Int. J. Hydrogen Energy*, 2015, **40**, 2963–2970.
68 G. I. Konstantinov, S. S. Kurdyumov, Y. V. Maksimov, O. V. Bukhtenko and M. V. Tsodikov, *Catal. Ind.*, 2018, **10**, 1–8.
69 A. Djaidja, H. Messaoudi, D. Kaddeche and A. Barama, *Int. J. Hydrogen Energy*, 2015, **40**, 4989–4995.
70 H. Provendier, C. Petit and A. Kiennemann, *C. R. Acad. Sci., Ser. IIc: Chim.*, 2001, **4**, 57–66.
71 R. Thalinger, M. Gocyla, M. Heggen, R. Dunin-Borkowski, M. Grünbacher, M. Stöger-Pollach, D. Schmidmair, B. Klötzer and S. Penner, *J. Catal.*, 2016, **337**, 26–35.
72 T. J. Huang, T. C. Yu and S. Y. Jhao, *Ind. Eng. Chem. Res.*, 2006, **45**, 15–156.
73 E. Nikolla, J. Schwank and S. Linic, *J. Catal.*, 2007, **250**, 85–93.
74 M. Nawfal, C. Gennequin, M. Labaki, B. Nsouli, A. Aboukaïs and E. Abi-Aad, *Int. J. Hydrogen Energy*, 2015, **40**, 1269–1277.
75 S. C. Baek, K. W. Jun, Y. J. Lee, J. D. Kim, D. Y. Park and K. Y. Lee, *Res. Chem. Intermed.*, 2012, **38**, 1225–1236.
76 S. Katheria, G. Deo and D. Kunzru, *Appl. Catal., A*, 2019, **570**, 308–318.
77 F. Morales-Cano, L. F. Lundegaard, R. R. Tiruvalam, H. Falsig and M. S. Skjøth-Rasmussen, *Appl. Catal., A*, 2015, **498**, 117–125.
78 D. Li, T. Shishido, Y. Oumi, T. Sano and K. Takehira, *Appl. Catal., A*, 2007, **332**, 98–109.
79 A. H. Dam, H. Wang, R. Dehghan-Niri, X. Yu, J. C. Walmsley, A. Holmen, J. Yang and D. Chen, *ChemCatChem*, 2019, **11**, 3401–3412.
80 H. Wang, D. W. Blaylock, A. H. Dam, S. E. Liland, K. R. Rout, Y.-A. Zhu, W. H. Green, A. Holmen and D. Chen, *Catal. Sci. Technol.*, 2017, **7**, 1713–1725.
81 Y. Xu, T. Hirano, H. Kunieda, Y. Hara and Y. Miyata, *Catal. Sci. Technol.*, 2020, **10**, 2004–2019.
82 L. Wang, *Bull. Mater. Sci.*, 2020, **43**, 1–3.
83 Z. Liu, F. Gao, Y. A. Zhu, Z. Liu, K. Zhu and X. Zhou, *Chem. Commun.*, 2020, **56**, 13536–13539.
84 V. K. Jaiswar, S. Katheria, G. Deo and D. Kunzru, *Int. J. Hydrogen Energy*, 2017, **42**, 18968–18976.
85 X. Li, D. Li, H. Tian, L. Zeng, Z. J. Zhao and J. Gong, *Appl. Catal., B*, 2017, **202**, 683–694.
86 S. Palma, L. F. Bobadilla, A. Corrales, S. Ivanova, M. A. Centeno and J. A. Odriozola, *Appl. Catal., B*, 2014, **144**, 846–854.
87 Y. H. Chin, D. L. King, H. S. Roh, Y. Wang and S. M. Heald, *J. Catal.*, 2006, **244**, 153–162.
88 F. M. Sapountzi, C. Zhao, A. Boréave, L. Retailleau-Mevel, D. Niakolas, C. Neofytidis and P. Vernoux, *Catal. Sci. Technol.*, 2018, **8**, 1578–1588.
89 Z. T. Wang, M. T. Darby, A. J. Therrien, M. El-Soda, A. Michaelides, M. Stamatakis and E. C. H. Sykes, *J. Phys. Chem. C*, 2016, **120**, 13574–13580.
90 Q. Shen, Y. Jiang, F. Xia, B. Wang, X. Lv, W. Ye and G. Yang, *Pet. Sci. Technol.*, 2020, **38**, 618–625.
91 R. Manabe, S. Okada, R. Inagaki, K. Oshima, S. Ogo and Y. Sekine, *Sci. Rep.*, 2016, **6**, 3–4.
92 S. Okada, R. Manabe, R. Inagaki, S. Ogo and Y. Sekine, *Catal. Today*, 2018, **307**, 272–276.
93 M. Torimoto, K. Murakami and Y. Sekine, *Bull. Chem. Soc. Jpn.*, 2019, **92**, 1785–1792.
94 M. Torimoto, S. Ogo, Y. Hisai, N. Nakano, A. Takahashi, Q. Ma, J. G. Seo, H. Tsuneki, T. Norby and Y. Sekine, *RSC Adv.*, 2020, **10**, 26418–26424.
95 A. Takahashi, R. Inagaki, M. Torimoto, Y. Hisai, T. Matsuda, Q. Ma, J. G. Seo, T. Higo, H. Tsuneki, S. Ogo, T. Norby and Y. Sekine, *RSC Adv.*, 2020, **10**, 14487–14492.
96 M. Torimoto, S. Ogo, D. Harjowinoto, T. Higo, J. G. Seo, S. Furukawa and Y. Sekine, *Chem. Commun.*, 2019, **55**, 6693–6695.
97 A. J. Najfach, C. B. Almquist and R. E. Edelmann, *Catal. Today*, 2021, **369**, 31–47.
98 Y. Ramezani, F. Meshkani and M. Rezaei, *J. Chem. Sci.*, 2018, **130**, 1–10.
99 K. Tomishige, D. Li, M. Tamura and Y. Nakagawa, *Catal. Sci. Technol.*, 2017, **7**, 3952–3979.
100 Z. Song, Q. Wang, C. Guo, S. Li, W. Yan, W. Jiao, L. Qiu, X. Yan and R. Li, *Ind. Eng. Chem. Res.*, 2020, **59**, 17250–17258.
101 T. Margossian, K. Larmier, S. M. Kim, F. Krumeich, C. Müller and C. Copéret, *ACS Catal.*, 2017, **7**, 6942–6948.
102 S. M. Kim, P. M. Abdala, T. Margossian, D. Hosseini, L. Foppa, A. Armutlulu, W. Van Beek, A. Comas-Vives, C.

Copéret and C. Müller, *J. Am. Chem. Soc.*, 2017, **139**, 1937–1949.
103 S. A. Theofanidis, V. V. Galvita, H. Poelman and G. B. Marin, *ACS Catal.*, 2015, **5**, 3028–3039.
104 G. Gunduz-Meric, S. Kaytakoglu and L. Degirmenci, *Int. J. Hydrogen Energy*, 2020, **45**, 34547–34556.
105 S. A. Theofanidis, V. V. Galvita, M. Sabbe, H. Poelman, C. Detavernier and G. B. Marin, *Appl. Catal., B*, 2017, **209**, 405–416.
106 L. Xu, H. Wen, X. Jin, Q. Bing and J. Liu, *Appl. Surf. Sci.*, 2018, **443**, 515–524.
107 K. Ray, A. S. Sandupatla and G. Deo, *Int. J. Quantum Chem.*, 2021, **121**, 1–7.
108 Y. Kim, H. S. Lim, M. Lee and J. W. Lee, *Catal. Today*, 2021, **368**, 86–95.
109 T. Zhang, Z. Liu, Y. A. Zhu, Z. Liu, Z. Sui, K. Zhu and X. Zhou, *Appl. Catal., B*, 2020, **264**, 118497.
110 S. A. Theofanidis, V. V. Galvita, H. Poelman, N. V. R. A. Dharanipragada, A. Longo, M. Meledina, G. Van Tendeloo, C. Detavernier and G. B. Marin, *ACS Catal.*, 2018, **8**, 5983–5995.
111 H. Wang, N. V. Srinath, H. Poelman, C. Detavernier, P. Li, G. B. Marin and V. V. Galvita, *Catal. Sci. Technol.*, 2020, **10**, 6987–7001.
112 S. Das, S. Bhattar, L. Liu, Z. Wang, S. Xi, J. J. Spivey and S. Kawi, *ACS Catal.*, 2020, **10**, 12466–12486.
113 S. Joo, O. Kwon, S. Kim, H. Y. Jeong and G. Kim, *J. Electrochem. Soc.*, 2020, **167**, 064518.
114 S. Joo, A. Seong, O. Kwon, K. Kim, J. H. Lee, R. J. Gorte, J. M. Vohs, J. W. Han and G. Kim, *Sci. Adv.*, 2020, **6**, 1–9.
115 S. Shah, S. Sayono, J. Ynzunza, R. Pan, M. Xu, X. Pan and K. L. Gilliard-AbdulAziz, *AIChE J.*, 2020, **66**, 1–12.
116 Z. Wu, B. Yang, S. Miao, W. Liu, J. Xie, S. Lee, M. J. Pellin, D. Xiao, D. Su and D. Ma, *ACS Catal.*, 2019, **9**, 2693–2700.
117 C. Jiang, E. Loisel, D. A. Cullen, J. A. Dorman and K. M. Dooley, *J. Catal.*, 2021, **393**, 215–229.
118 A. Beheshti Askari, M. Al Samarai, B. Morana, L. Tillmann, N. Pfänder, A. Wandzilak, B. Watts, R. Belkhou, M. Muhler, M. Muhler and S. Debeer, *ACS Catal.*, 2020, **10**, 6223–6230.
119 A. Beheshti Askari, M. Al Samarai, N. Hiraoka, H. Ishii, L. Tillmann, M. Muhler and S. Debeer, *Nanoscale*, 2020, **12**, 15185–15192.
120 D. Harshini, Y. Kwon, J. Han, S. P. Yoon, S. W. Nam and T.-H. Lim, *Korean J. Chem. Eng.*, 2010, **27**, 480–486.
121 A. Movasati, S. M. Alavi and G. Mazloom, *Fuel*, 2019, **236**, 1254–1262.
122 H. Wang, X. Dong, T. Zhao, H. Yu and M. Li, *Appl. Catal., B*, 2019, **245**, 302–313.
123 S. Das, M. Sengupta, A. Bag, M. Shah and A. Bordoloi, *Nanoscale*, 2018, **10**, 6409–6425.
124 K. Sheng, D. Luan, H. Jiang, F. Zeng, B. Wei, F. Pang and J. Ge, *ACS Appl. Mater. Interfaces*, 2019, **11**, 24078–24087.
125 T. J. Siang, S. Singh, O. Omoregbe, L. G. Bach, N. H. H. Phuc and D. V. N. Vo, *J. Energy Inst.*, 2018, **91**, 683–694.
126 H. Ghanbarabadi and B. Khoshandam, *Int. J. Environ. Anal. Chem.*, 2021, DOI: 10.1080/03067319.2020.1862812, in press.
127 K. Cao, M. Gong, J. Yang, J. Cai, S. Chu, Z. Chen, B. Shan and R. Chen, *J. Catal.*, 2019, **373**, 351–360.
128 J. Horlyck, C. Lawrey, E. C. Lovell, R. Amal and J. Scott, *Chem. Eng. J.*, 2018, **352**, 572–580.
129 X. Zhang, Z. Vajglova, P. Mäki-Arvela, M. Peurla, H. Palonen, D. Y. Murzin, S. A. Tungatarova, T. S. Baizhumanova and Y. A. Aubakirov, *ChemistrySelect*, 2021, **6**, 3424–3434.
130 A. S. Al-Fatesh, J. K. Abu-Dahrieh, H. Atia, U. Armbruster, A. A. Ibrahim, W. U. Khan, A. E. Abasaeed and A. H. Fakeeha, *Int. J. Hydrogen Energy*, 2019, **44**, 21546–21558.
131 Z. Bian and S. Kawi, *J. CO2 Util.*, 2017, **18**, 345–352.
132 G. Gunduz-Meric, S. Kaytakoglu and L. Degirmenci, *React. Kinet., Mech. Catal.*, 2020, **129**, 403–419.
133 J. Xin, H. Cui, Z. Cheng and Z. Zhou, *Appl. Catal., A*, 2018, **554**, 95–104.
134 H. Wu, J. X. Liu, H. Liu and D. He, *Fuel*, 2019, **235**, 868–877.
135 Y. Turap, I. Wang, T. Fu, Y. Wu, Y. Wang and W. Wang, *Int. J. Hydrogen Energy*, 2020, **45**, 6538–6548.
136 M. A. Vasiliades, P. Djinović, A. Pintar, J. Kovač and A. M. Efstathiou, *Catal. Sci. Technol.*, 2017, **7**, 5422–5434.
137 P. Djinović and A. Pintar, *Appl. Catal., B*, 2017, **206**, 675–682.
138 Y. Wei, M. Song, L. Yu and F. Meng, *Process Saf. Environ. Prot.*, 2021, **145**, 236–246.
139 T. S. Phan, A. R. Sane, B. Rêgo de Vasconcelos, A. Nzihou, P. Sharrock, D. Grouset and D. Pham Minh, *Appl. Catal., B*, 2018, **224**, 310–321.
140 U. Guharoy, E. Le Saché, Q. Cai, T. R. Reina and S. Gu, *J. CO2 Util.*, 2018, **27**, 1–10.
141 F. de A. R. da Silva, R. C. R. dos Santos, R. S. Nunes and A. Valentini, *Appl. Catal., A*, 2021, **618**, 118129.
142 K. Song, M. Lu, S. Xu, C. Chen, Y. Zhan, D. Li, C. Au, L. Jiang and K. Tomishige, *Appl. Catal., B*, 2018, **239**, 324–333.
143 A. Chatla, M. M. Ghouri, O. W. El Hassan, N. Mohamed, A. V. Prakash and N. O. Elbashir, *Appl. Catal., A*, 2020, **602**, 117699.
144 R. Rezaei, G. Moradi and S. Sharifnia, *Energy Fuels*, 2019, **33**, 6689–6706.
145 K. Han, S. Wang, Q. Liu and F. Wang, *ACS Appl. Nano Mater.*, 2021, **4**, 5340–5348.
146 M. Wang, T. Zhao, M. Li and H. Wang, *RSC Adv.*, 2017, **7**, 41847–41854.
147 S. Sokolov, J. Radnik, M. Schneider and U. Rodemerck, *Int. J. Hydrogen Energy*, 2017, **42**, 9831–9839.
148 S. M. Masoom Nataj, S. M. Alavi and G. Mazloom, *J. Chem. Technol. Biotechnol.*, 2019, **94**, 1305–1314.
149 L. Yao, M. E. Galvez, C. Hu and P. Da Costa, *Int. J. Hydrogen Energy*, 2017, **42**, 23500–23507.
150 L. Yao, M. E. Galvez, C. Hu and P. Da Costa, *Ind. Eng. Chem. Res.*, 2018, **57**, 16645–16656.
151 Y. Song, E. Ozdemir, S. Ramesh, A. Adishev, S. Subramanian, A. Harale, M. Albuali, B. A. Fadhel, A. Jamal, D. Moon, S. H. Choi and C. T. Yavuz, *Science*, 2020, **367**, 777–781.

152 W. Liu, L. Li, S. Lin, Y. Luo, Z. Bao, Y. Mao, K. Li, D. Wu and H. Peng, *J. Energy Chem.*, 2022, **65**, 34–47.
153 J. Károlyi, M. Németh, C. Evangelisti, G. Sáfrán, Z. Schay, A. Horváth and F. Somodi, *J. Ind. Eng. Chem.*, 2018, **58**, 189–201.
154 M. A. Álvarez, L. F. Bobadilla, V. Garcilaso, M. A. Centeno and J. A. Odriozola, *J. CO2 Util.*, 2018, **24**, 509–515.
155 I. Luisetto, C. Sarno, D. De Felicis, F. Basoli, C. Battocchio, S. Tuti, S. Licoccia and E. Di Bartolomeo, *Fuel Process. Technol.*, 2017, **158**, 130–140.
156 I. Wysocka, J. Hupka and A. Rogala, *Catalysts*, 2019, **9**, 540.
157 H. Zhou, T. Zhang, Z. Sui, Y. A. Zhu, C. Han, K. Zhu and X. Zhou, *Appl. Catal., B*, 2018, **233**, 143–159.
158 T. Mozammel, D. Dumbre, R. Hubesch, G. D. Yadav, P. R. Selvakannan and S. K. Bhargava, *Energy Fuels*, 2020, **34**, 16433–16444.
159 P. N. Romano, J. F. S. de Carvalho Filho, J. M. A. R. de Almeida and E. F. Sousa-Aguiar, *Catal. Today*, 2021, DOI: 10.1016/j.cattod.2021.08.006, in press.
160 D. Zubenko, S. Singh and B. A. Rosen, *Appl. Catal., B*, 2017, **209**, 711–719.
161 B. T. Egelske, J. M. Keels, J. R. Monnier and J. R. Regalbuto, *J. Catal.*, 2020, **381**, 374–384.
162 M. A. Vasiliades, C. M. Damaskinos, K. K. Kyprianou, M. Kollia and A. M. Efstathiou, *Catal. Today*, 2020, **355**, 788–803.
163 W. Y. Kim, J. S. Jang, E. C. Ra, K. Y. Kim, E. H. Kim and J. S. Lee, *Appl. Catal., A*, 2019, **575**, 198–203.
164 N. A. K. Aramouni, J. Zeaiter, W. Kwapinski, J. J. Leahy and M. N. Ahmad, *Fuel*, 2021, **300**, 120950.
165 F. Jin, Y. Fu, W. Kong, J. Wang, F. Cai, J. Zhang and J. Xu, *Chem. Phys. Lett.*, 2020, **750**, 137491.
166 S. S. Itkulova, Y. Y. Nurmakanov, S. K. Kussanova and Y. A. Boleubayev, *Catal. Today*, 2018, **299**, 272–279.
167 M. C. J. Bradford and M. A. Vannice, *Catal. Rev.: Sci. Eng.*, 1999, **41**, 1–42.
168 D. San-José-Alonso, J. Juan-Juan, M. J. Illán-Gómez and M. C. Román-Martínez, *Appl. Catal., A*, 2009, **371**, 54–59.
169 Z. Xie, B. Yan, S. Kattel, J. H. Lee, S. Yao, Q. Wu, N. Rui, E. Gomez, Z. Liu, W. Xu, L. Zhang and J. G. Chen, *Appl. Catal., B*, 2018, **236**, 280–293.
170 F. Touahra, R. Chebout, D. Lerari, D. Halliche and K. Bachari, *Energy*, 2019, **171**, 465–474.